Tuning the 3D microenvironment of reprogrammed tubule cells enhances biomimetic modeling of polycystic kidney disease

Roman Pichler [a,1], Ludovica Rizzo [b,c,1], Kevin Tröndle [d], Michaela Bühler [a], Hanna Brucker [a], Anna-Lena Müller [a], Kelli Grand [b], Silvia Farè [e], Amandine Viau [a], Michael M. Kaminski [f,g,h], E. Wolfgang Kuehn [a], Fritz Koch [d], Stefan Zimmermann [d], Peter Koltay [d], Soeren S. Lienkamp [a,b,*]

[a] Department of Medicine IV, Medical Center - University of Freiburg, Faculty of Medicine, University of Freiburg, Freiburg, Germany
[b] Institute of Anatomy, University of Zurich, Zurich, Switzerland
[c] Molecular and Translational Biomedicine PhD Program, Life Science Zurich Graduate School, Zurich, Switzerland
[d] Laboratory for MEMS Applications, IMTEK - Department of Microsystems Engineering, University of Freiburg, Freiburg, Germany
[e] Department of Chemistry, Materials and Chemical Engineering "G. Natta", Politecnico di Milano, Milan, Italy
[f] Berlin Institute for Medical Systems Biology, Max Delbrück Center for Molecular Medicine in the Helmholtz Association, 10115 Berlin, Germany
[g] Department of Nephrology and Medical Intensive Care, Charité Universitätsmedizin Berlin, 10117 Berlin, Germany
[h] Berlin Institute of Health, Berlin, Germany

ARTICLE INFO

ABSTRACT

Renal tubular cells frequently lose differentiation markers and physiological properties when propagated in conventional cell culture conditions. Embedding cells in 3D microenvironments or controlling their 3D assembly by bioprinting can enhance their physiological properties, which is beneficial for modeling diseases *in vitro*.

A potential cellular source for modeling renal tubular physiology and kidney diseases *in vitro* are directly reprogrammed induced renal tubular epithelial cells (iRECs). iRECs were cultured in various biomaterials and as bioprinted tubular structures. They showed high compatibility with the embedding substrates and dispensing methods. The morphology of multicellular aggregates was substantially influenced by the 3D microenvironment. Transcriptomic analyses revealed signatures of differentially expressed genes specific to each of the selected biomaterials. Using a new cellular model for autosomal-dominant polycystic kidney disease, $Pkd1^{-/-}$ iRECs showed disrupted morphology in bioprinted tubules and a marked upregulation of the Aldehyde dehydrogenase 1a1 (*Aldh1a1*). In conclusion, 3D microenvironments strongly influence the morphology and expression profiles of iRECs, help to unmask disease phenotypes, and can be adapted to experimental demands. Combining a direct reprogramming approach with appropriate biomaterials will facilitate construction of biomimetic kidney tubules and disease models at the microscale.

1. Introduction

The incidence of kidney disease is increasing globally, and there is an urgent demand for new diagnostic and therapeutic options. Kidney diseases can be modeled in animals, but for many applications, such as biochemical analysis, screens or drug candidate identification, *in vitro* models are more suitable to uncover pathophysiological mechanisms and identify new therapeutic targets. Primary renal derived cells are difficult to keep differentiated in culture and stable cell lines tend to lose their kidney-specific properties after immortalization [1–4]. An

alternative cellular model are induced renal tubular epithelial cells (iRECs), obtained by directly reprogramming mouse and human fibroblasts using 4 transcription factors (Hnf1b, Pax8, Hnf4a, Emx2) [5]. iRECs can be cultured for months without changes to their differentiation state, and they retain many functional properties of renal tubular cells [5,6]. iRECs have been mainly employed in 2D assays, but their behavior in 3D microenvironments and their potential to model renal diseases have not yet been explored [5].

In contrast to conventionally plated culture techniques, 3D culture allows cells to freely grow and migrate without being constricted to a

---

single plane, and significantly changes cellular morphology, cell-cell and cell-matrix interactions [7–9]. These effects are mediated by transcriptional changes, and thus provide stimuli that enhance physiological properties of cells. For instance, 3D cultured hepatocytes re-acquired the ability to store glycogen, produced bile salts, and showed enhanced expression of liver-specific proteins in contrast to conventional 2D cultures [10]. Similarly, by tuning the 3D microenvironment, the transcriptional signature of stem cell-derived neurons was shifted towards specific cerebral subregions at different developmental stages [11]. How changing culture conditions from 2D to 3D affects renal tubular cells, and reprogrammed iRECs in particular, has not been systematically analyzed.

A large variety of embedding techniques and biomaterials is available to generate suitable 3D microenvironments and improved culture conditions for different tissue types [12–14]. The kidney is considered a soft organ with a shear modulus of about 4.5 kPa, measured by magnetic resonance elastography [15], thus natural biomaterials are most suitable to support renal tubular cells [16]. Hydrogels represent modifiable networks of hydrophilic polymer chains in a water rich environment [17], and closely mimic the native extracellular matrix (ECM). The renal ECM is rich in collagen I and collagen IV [18]. Laminin and smaller molecules like entactin and other sulfated proteoglycans bridge the collagen fibrils and form a 3D network. Materials like Matrigel, mainly composed of laminin and collagen IV, are feasible candidates to reconstruct a kidney-like ECM [19]. Collagen I, fibrin and alginate are biomaterials widely employed to generate biomimetic 3D cell culture models [20,21]. For example, advanced micro-patterned microenvironments have been bioprinted using alginate [20]. Bioprinting can deliver highly reproducible results, but it requires the biomaterials to be finely adapted to each dispensing technique [22]. Despite recent advances, it remains a great challenge to fabricate functional renal tissues and tubular constructs [21,23]. We recently established a Drop-on-Demand (DoD) bioprinting process to generate defined patterns of iRECs in hydrogels and utilized their self-organizational properties to achieve tubular structures with a mean diameter of 105 ± 22 μm [24]. The physiological properties of iREC tubules have not been explored, nor has bioprinting been applied to model tubular kidney diseases.

Autosomal-dominant polycystic kidney disease (ADPKD) is the most prevalent monogenetic kidney disorder, affecting over 12 million patients worldwide [25] and leading to progressive kidney failure and end-stage renal disease [26]. The only approved treatment (Tolvaptan) delays disease progression by targeting cAMP mediated re-absorption in the collecting ducts, but it elicits thirst and increased diuresis, as well as liver toxicity, as prevalent side effects [27]. ADPKD is mainly caused by mutations of either *PKD1* or *PKD2*. While inflammation and fibrosis contribute to subsequent renal failure, the primary insult that triggers cyst formation is a somatic "second hit" mutation of one of these genes in tubular epithelial cells [28,29]. Most mouse models of ADPKD only partially replicate the clinical phenotype of patients, as truly orthologous heterozygous knockout mice have a mild renal phenotype [30]. Cellular models for ADPKD exist, but are limited by diminished differentiation, or lack of isogenic controls [31]. Embedding cells in a 3D matrix of either collagen I [32] or Matrigel [33] elicits micro-cyst formation in spheroids. Interestingly, cAMP stimulation is required to trigger cyst formation *in vitro* in most cases. However, cysts also form in wild-type cells, though to a lesser degree than in *PKD1/PKD2* deficient cells. These models are well suited but largely restricted to studying the role of cAMP dependent cyst progression driven by fluid secretion in the collecting duct, as no cysts are observed in the absence of cAMP agonists [32]. The positioning of seeded cells is hard to control and constructs generally do not assume a tubular architecture. iPSC-derived renal organoids have been generated that harbor mutations in *PKD1* and *PKD2* and form cystic expansion spontaneously [34,35]. However, due to the heterogeneous nature of organoids, effects of loss of PKD1 or PKD2 specifically on tubular cells are hard to distinguish from secondary factors that aggravate cyst progression and tubular injury, such as microenvironmental cues or fibrosis [34–37].

Therefore, iRECs represent an attractive cell culture and disease model because they maintain a state of differentiation when cultured and passaged extensively. They represent a tubular cell model that can be experimentally evaluated in isolation. Direct effects on the epithelium can be evaluated excluding the confounding effects of fibrosis and inflammation. Here, we investigated the impact of 3D microenvironments on iRECs by analyzing combinations of kidney ECM-like biomaterials and dispensing techniques. We assessed the physiological properties of cellular structures promoted by each microenvironment, including cell viability, morphology, and changes in gene expression. We detected gene signatures specific for each microenvironment and dispensing technique. Furthermore, using Cre recombinase mediated *Pkd1* knockout, we generated an *in vitro* ADPKD model, which uncovered an overabundance of *Aldh1a1* expression. Bioprinted tubule-like structures of *Pkd1*$^{-/-}$ cells showed disrupted tubular integrity and outgrowth of radial side branches. Thus, microenvironmental conditions strongly influence the proliferative status, morphology, and gene expression profile of iRECs that may inform future experimental design strategies. In addition, *Pkd1*$^{-/-}$ iRECs uncover a potential role for *Aldh1a1* in ADPKD, and bioprinted tubular arrays are suitable for modeling cystic kidney disease *in vitro*.

2. Materials and methods

2.1. Animals

For *Pkd1*$^{flox/flox}$ (*Pkd1*$^{fl/fl}$) mouse embryonic fibroblast (MEF) isolation, homozygous E13.5 mouse embryos of B6.129S4-Pkd1^{tm2Ggg}/J mice were sacrificed [38]. For RNA experiments, *Pkd1*$^{fl/fl}$;Pax8^{rtTA};TetO-cre mice received doxycycline hydrochloride via the drinking water (2 mg ml^{-1} with 5% sucrose, protected from light) from postnatal day 28 (P28) to P42 to develop polycystic kidney disease, as previously described (iPkd1) [39]. Littermates (lacking either TetOCre or Pax8rtTA) were used as controls. Experiments were conducted on males. The mice were sacrificed at 12 weeks of age.

All animals were raised in a SPF facility with a 12 h day/night cycle and free access to water and chow. Experiments were conducted in accordance with the National Institutes of Health Guide for the Care and Use of Laboratory Animals and the German law for the welfare of animals (Regierungspräsidium Freiburg). Primers used for genotyping are listed in Supplementary Table 1.

2.2. Cloning and virus production

The coding sequences of mouse transcription factors *Pax8*, *Emx2*, *Hnf1b* and *Hnf4a* were cloned into the pWPXLd lentiviral vector (Addgene, #12258). Cre recombinase was cloned from cre-NLS-p3-26 (kind gift from the European Xenopus Resource Centre) and Flp recombinase (optimized Flippase) from pDIRE (Addgene, #26745). The puromycin resistance was cloned from pLIX_403 (Addgene, #41395). Cre and Flp were combined with puromycin resistance and cloned into the pWPXLd vector for lentiviral expression (Cre-Puro and Flp-Puro). The *Pkd1*-containing pLXSN retroviral transfer vector was a kind gift by Tilman Busch and Michael Koettgen, University Clinic Freiburg. Here, the coding sequence of *Pkd1*, flanked by n-terminal Flag and c-terminal V5 tag, was cloned into the pLXSN retroviral transfer vector. For production of lentivirus, three plasmids (pWPXLd; psPax2, Addgene, #12260; pMD2.G, Addgene, #12259) were transfected into HEK293T cells (ATCC®, HEK 293 T/17, CRL-11268). Virus concentration and harvest were performed as previously described [40] using polyethylene 6000 precipitation and ultracentrifugation at 6800 rpm. Analogously, for γ-retrovirus production the transfer vector pLXSN, the packaging vector pMD-MLV Gag/Pol and the envelope-containing vector pMDG VSV-G were co-transfected into HEK293T cells, and the same protocol of virus concentration was applied.

2.3. Cell culture

Induced renal tubular epithelial cells (iRECs) were developed by Kaminski et al. by direct reprogramming of mouse embryonic fibroblasts (MEFs) by transduction of the four transcription factors *Emx2*, *Hnf1b*, *Hnf4a*, and *Pax8* [5]. Cells were cultured in MEF medium (MEFM), containing standard Dulbecco's modified Eagle's medium (Gibco, DMEM, 41966029), supplemented with 10% v/v fetal bovine serum (Sigma-Aldrich, FBS, F9665), 2 U l^{-1} penicillin/streptomycin (Sigma-Aldrich, P4333), and 2 mM L-glutamine (Gibco, 25030024). Where stated, iREC samples were cultured in Renal Epithelial Growth Medium (Lonza, REGM, CC-3190). MEFs were isolated from E13.5 embryos. Limbs and tail were cut, minced with a scalpel and trypsinized in 0.25% Trypsin-EDTA (Gibco) for 30 min. Cell pellets were resuspended in MEF medium, plated on 0.1% gelatin-coated cell culture dishes, and grown until confluency. $Pkd1^{fl/fl}$ iRECs were reprogrammed analogously to iRECs. In short, $Pkd1^{fl/fl}$ MEFs were transduced with four lentiviruses, each containing one of the four transcription factors *Pax8*, *Hnf1b*, *Hnf4a* and *Emx2*. The concentrated lentiviruses were diluted 1:100 to 1:200 in MEFM containing 10 μg ml^{-1} polybrene (Santa Cruz Biotechnology, sc-134220), and were transduced for 12 h for six consecutive days. Three weeks after lentiviral transduction, cells were singled in a FACSAria™ Fusion cell sorter (Becton Dickinson) and grown clonally in 96 well plates. After morphological and qPCR-based characterization each selected iREC clone was transduced with either a Flippase-Puromycin (Flp)- containing lentivirus (control cells) or a Cre-Puromycin (Cre)-containing lentivirus (*Pkd1* knockout cells) for three consecutive days. Cells were cryoconserved in freezing medium, containing 50% MEFM, 40% FBS, and 10% DMSO, and stored in liquid nitrogen. During cultivation, all cells were incubated in a humid atmosphere at 37 °C containing 5% CO_2. For RNA sequencing experiments, 3 *Pkd1* clone pairs (Flp and Cre transduced conditions) were seeded at an initial density of $1 \cdot 10^6$ cells in 10 cm dishes in MEFM. After confluency, cells were harvested for RNA extraction. For measurement of proliferation rates, $5 \cdot 10^4$ cells of *Pkd1* clones were seeded per 12-well hole on day 0. Starting at day 1, cell number was counted in triplicates for 7 consecutive days.

2.4. Hydrogel preparation and embedding

Materials purchased as lyophilized powder (fibrinogen, Merck, REF 341576; alginate, Sigma-Aldrich, Cas. No A0682; RGD-alginate, Novamatrix, NOVATACH VLVG 4GRGDSP, no. 4270519; calcium chloride, Sigma-Aldrich, Cas No 223506; aprotinin, Sigma-Aldrich A1153) and ready to use solutions (Matrigel® growth factor reduced, Corning, REF 354230; collagen I, Corning, REF 354236) were dissolved, stored and handled as stated by manufacturers. Briefly, trypsinized and singled iRECs were resuspended in the different hydrogel precursors for a final concentration of $1.0–1.5 \cdot 10^5$ cells ml^{-1} and a volume of 40 μl per sample (i.e., 4000–6000 cells per sample). The gelling procedure was performed as stated by the manufacturers, and each replicate was dispensed in one well of a μ-slide 8 well dish (ibidi®, Cat. No. 80826). In brief, cell pellets were resuspended in Matrigel solutions (final concentration of 6 mg ml^{-1}) or 3 mg ml^{-1} collagen I neutralized with 10x PBS, dH_2O and NaOH 1 N (Sigma-Aldrich, REF S2770). Fibrin hydrogels were obtained by resuspending iREC pellets in 10 mg ml^{-1} fibrinogen, plating 20 μl per well and cross-linking them enzymatically with 20 μl of 5 U ml^{-1} thrombin (Calbiochem, REF 605157). All samples were incubated at 37 °C for 20 min prior to addition of culture media (MEFM or REGM), with aprotinin for the fibrin condition. Alginate and RGD-alginate solutions were obtained dissolving 1 mg or 2 mg alginate powder in 100 ml dH_2O, for 1% and 2% w/v solutions respectively. To form alginate hydrogels, the cross-linking agent calcium chloride was dissolved in dH_2O and alginate solutions were cross-linked with 10% w/v calcium chloride for biomaterial characterizations, or 2%, 5% or 10% w/v calcium chloride for bioprinting experiments. For cell encapsulation, iREC pellets were resuspended in 2% w/v alginate or RGD-alginate solutions and utilized directly for bioprinting, separately loaded in the inkjet bioprinter from the calcium chloride solution.

For 3D cell culture of *Pkd1* iRECs in Matrigel, cells were passed through a 50 μm cell strainer to avoid cell aggregates, counted to yield a final cell concentration of 100 cells $μl^{-1}$, and resuspended in Matrigel at 4 °C (final concentration of 6 mg ml^{-1}). Cell suspensions in Matrigel were incubated at 37 °C in 8 well ibidi® dishes (ibidi®) for 20 min to allow thermally induced gelification. Afterwards, hydrogels were incubated in REGM for up to 10 days before staining. Flp- and Cre-transduced *Pkd1* clones were embedded in parallel, n = 6 clones. For hanging drop culture, *Pkd1* iRECs were used at a concentration of 25 cells $μl^{-1}$ in REGM containing 2.4 mg ml^{-1} methylcellulose. 64 drops (8 × 8) with a volume of 20 μl were pipetted onto the inner side of the lid of a 10 cm cell culture dish. Lids were carefully turned and hanging drops were cultured in a humidified atmosphere for 6 days.

2.5. Biomaterial characterization

All biomaterials were characterized by applying various tests on cross-linked samples (volume of 150 μl). Hydrogels were prepared (Matrigel®, fibrin, collagen I and alginate) and exposed to cell culture medium (DMEM). All conditions were weighed with a high precision scale, after removing the excess of solvent with adsorbent laboratory paper. The initial weight of each sample was registered as $weight_0$. Then, samples were weighed at referred time points until complete degradation ($weight_t$). Degradation was quantified by weight loss over time, $\Delta weight$, using formula (1):

$$\Delta_{weight} = 100 + (weight_t - weight_{t0}) / weight_{t0} \times 100 \tag{1}$$

Alginate hydrogels were further characterized with a dynamic mechanical analyzer (DMA Q800 T A. Instruments). Cylindrical samples (diameter = 5 mm, height = 2 mm, n = 3) were assessed using an unconfined compression test in physiological conditions (i.e., wet environment, 37 °C), applying a force ramp of 0.2 N min^{-1} until rupture. From the obtained curves stress values at 50% deformation ($\sigma_{50\%}$), the maximum reached strain (ε_{max}), and the related maximum stress (σ_{max}) were compared for the two sample types.

In addition, viscosity measurements of 1% w/v alginate, 2% w/v alginate and 2% w/v RGD-alginate solutions were conducted prior to crosslinking, in absence of calcium chloride solution, with a rotational rheometer (MCR 52 Anton Paar GmbH, Austria). Measurements were carried out at room temperature (T_{room} = 24 °C), with a cone plate geometry (gap = 96 μm, $\alpha_{cone-plate}$ = 0.997°, φ_{cone} = 49.966 mm). The viscosity was assessed in relation to the shear rate (1–19000 s^{-1}). The working shear rate was estimated according to the printing parameters [41]. With a nozzle diameter of 500 μm and an outlet velocity of 2 m s^{-1}, the estimated shear rate was 8000 s^{-1}. This value was used to infer the viscosity of alginate solutions.

2.6. Immunofluorescence staining and viability assays

Cell viability was determined with a live/dead assay, using ReadyProbes™ Cell Viability Imaging Kit, Blue/Red (Thermo Fisher Scientific, REF R37610) to stain cell nuclei with DAPI and dead cell nuclei with propidium iodide, according to manufacturer instructions. In short, samples were washed in 1x PBS and exposed to the staining solution for 25 min (65 μl of staining dye per 1 ml of DMEM). To measure intensities for dead cells, positive control samples were either frozen at −20 °C overnight in medium without DMSO (alginate and RGD-alginate) or exposed to 4% PFA before staining. The impact of the bioprinting process on cell viability was evaluated via a live/dead assay using inkjet bioprinted and manually dispensed iREC suspensions at a concentration of $1.68 \cdot 10^5$ cells ml^{-1}, directly into 8-well ibidi dishes, pre-filled with 250 μl MEFM. Cell viability was measured at day 1, 3 and 7 after seeding.

For immunofluorescence experiments, samples were washed with PBS containing magnesium/calcium supplement, fixed in 4% para-formaldehyde for 30 min (except for ZO-1 staining, which was fixed in 100% methanol at 4 °C) and permeated with 0.5% Triton®X-100 (Carl Roth, Art. No. 3051.2). After incubation in blocking solution (5% BSA, 0.5% Tween20, 2% horse serum and 1% cold water fish skin gelatin in PBS) for 2 h, samples were stained with primary antibody, or a 1:100 dilution of Alexa Fluor™ 488 Phalloidin (Invitrogen, A-12379) or Phalloidin FluoProbes 647 (Interchim, FP-BA0320), at 4 °C overnight. After washing three times, samples were stained with the secondary antibody for 2 h, followed by 5–10 µg ml^{-1} Hoechst (Cayman, 16756) for 10–20 min. Last, after washing again for three times, samples were mounted in ibidi® mounting medium (ibidi®, Cat. No. 50001). Antibodies used for immunolabeling are listed in Supplementary Table 2.

2.7. Imaging

Imaging for live/dead assay and morphology was carried out with either an Apotome2 Zeiss, Colibri 2, Power Supply 232, Zeiss Axio Observer Z1, with a 20× air objective, or a confocal system NLO-I-LSM Zeiss LSM 880, with a 25× air objective.

Acquisitions of proliferation behaviors via pHH3 staining and ZO-1 localization were performed on the confocal SP8 Falcon 25× glycerol objective (10 Z-stacks per each triplicate and control), and three 80 µm Z-stacks per biological replicate, respectively. The validation of transcriptomic analyses was imaged with the Olympus Spinning disk with a 20× air or 30× oil objective, acquiring three 80 µm Z-stacks for each triplicate and control. Single frames of WT mouse kidney cryosections were imaged at a Leica DMI 6000 with a 40× oil objective. Images of Matrigel® embedded and DoD bioprinted *Pkd1* iRECs were made with a confocal laser scanning microscope (Zeiss, LSM 510 DUO with inverted microscope Axiovert 200) or a Zeiss Axio Observer.Z1 with ApoTome.2 ZEN and ZEN 2010 software. Bright-field images of hanging drop culture were taken with a Zeiss Axio Imager.M2 upright microscope. For second harmonic generation imaging, cells were pipetted manually onto a first collagen I layer instead of bioprinting to obtain less localized cell patterns before a second covering layer of collagen I was applied, and imaged at the multiphoton Leica SP8 MP DIVE FALCON, as previously described [42].

2.8. Image analysis

A custom-made code was developed with Fiji software (version 1.52p) to analyze images of live/dead assay experiments. Each acquired set of images consisted of image stacks in z direction and 3 fluorescence channels. First, the original multichannel images were split into separate stacks per fluorescence channel. A duplicate of the blue fluorescence channel was processed to detect the ROIs (regions of interest): nuclei of both living and dead cells stained with DAPI. All ROI positions were collected and overlapped to the unprocessed DAPI images at the corresponding z level to verify the correct nuclei detection. As further quality control of the automated segmentation, ROIs were overlapped to corresponding GFP images to check if each region was actually surrounded by cell surfaces, which express green fluorescent protein intrinsically in iRECs. Last, the detected ROIs were overlapped to the corresponding red fluorescence images to measure the median red intensity of each ROI and to assess cell viability with respect to positive control images. If the median red intensity value was lower than the average median red intensity of positive control data, that single cell was counted as a living cell, and vice versa. The quantitative analysis of iREC morphology in 3D was performed manually with imageJ, reporting the number of structures per z-stack, the number of cells composing each structure, the area at the largest aggregate diameter, and the respective circularity (range 0–1, perfect circle = 1).

The analysis of proliferating iRECs embedded in Matrigel, fibrin and collagen I was performed by processing acquired z-stacks with Imaris

software (Oxford Instruments Group) for nuclei segmentation (Hoechst channel). Each nucleus that showed a staining in the pHH3 channel was manually counted as a proliferating cell. Images of *Pkd1* iRECs were analyzed with Fiji ImageJ and images of iREC spheroids were further processed with Imaris software (Oxford Instruments Group). The orientation of actin filaments was performed with the Fiji plugin OrientationJ Analysis, as previously described [43].

2.9. Bioprinting

The bioprinting was performed using a Drop-on-Demand (DoD) technology based on a commercial piezo-driven dispenser (Biofluidix GmbH, PipeJet®, Germany). The dispenser used disposable sterile capillaries, which could be directly connected to pipette-tips as bioink reservoirs. This allowed voxelated deposition of single bioink droplets with adjustable volumes between 1 and 70 nl, using a nozzle diameter of 200 or 500 µm. Detailed descriptions of the bioprinting process can be found below [24,44].

2.10. Micropatterned alginate single- and multilayer substrates

First, single-layer alginate substrates were optimized by printing calcium chloride droplets varying D_x (distance between consecutive drops) along the same line and D_y (distance between parallel lines) for parallel lines, and by changing droplet dimension depending on the chosen nozzle diameter $Ø_{nozzle}$. Multilayer iRECs-laden alginate samples were bioprinted with a single 10 mm line geometry. Distance between consecutive droplets met 50% nozzle size, so that droplets overlapped about 50% ($D_x = Ø_{nozzle}/2 = 250$ µm). The final sample was obtained by overlapping 5 hydrogel layers, composed of iRECs-laden alginate bioprinted with a 0.5 mm nozzle diameter. On top of each layer a 5% w/v $CaCl_2$ solution was bioprinted with a 0.2 mm nozzle diameter. For improved stability in height and hydrogel crosslinking, a waiting time of 60 s elapsed between each consecutive layer.

2.11. Bioprinted tubule in collagen/fibrin sandwich

To mimic the complex structure of the kidney extracellular matrix, we produced bioprinted samples combining two biomaterials (collagen I and fibrin). Cell growth was supported by bioprinting a high density iRECs-laden fibrinogen bioink in a line pattern on top of a collagen I layer as substrate. To stabilize the construct, a second collagen I layer was pipetted on top.

In detail, collagen I (Corning, collagen I, rat tail, REF 354236) was pipetted on a glass coverslip to form the first hydrogel layer. Collagen I was used at a final concentration of 3 mg ml^{-1} and was mixed with thrombin (Calbiochem, thrombin, human plasma, final concentration 10 U ml^{-1}, #605190), required for the crosslinking of the upcoming fibrinogen layer. The pH of the solution was brought to alkalinity by adding sodium hydroxide (NaOH, 1 M), double distilled water, and PBS (Sigma-Aldrich, PBS, 10X) to allow gelification of collagen I. Crosslinking was thermally induced by incubation at 37 °C for 30 min. Cells were suspended in fibrinogen (Calbiochem, fibrinogen, human plasma, final concentration 5 mg ml^{-1}, #341576) as a carrier at a concentration of 1.5· 10^7 cells ml^{-1} (adjustable concentration range of 1· 10^6 to 2.5· 10^7 cells ml^{-1}, leading to droplets containing 10 to 250 cells, respectively). The cell suspension was deposited as droplets (volume of 10 nl) by the piezo-driven DoD dispenser (nozzle diameter 200 µm). Fibrinogen was cross-linked by thrombin, contained in the first hydrogel layer, to form on-site cell patterns and a fixed fibrin scaffold. Single droplets were combined by overlap printing to form a continuous line with a droplet-to-droplet distance of 200 µm. The freshly bioprinted cell pattern was then covered with a second collagen I layer (3 mg ml^{-1}) for encapsulation. Bioprinted cells were incubated in REGM for up to 10 days. To avoid enzymatic digestion of fibrin by cell secreted proteases, aprotinin was added to cell culture medium (Sigma, aprotinin, bovine

lung, 20 µg ml^{-1}, A1153). During incubation in REGM cell aggregates self-assembled and developed into a single tubular structure. Cell compatibility with the printing process and iREC viability were assessed by applying ReadyProbes™ Cell Viability Imaging Kit, Blue/Red (Thermo Fisher Scientific) to stain cell nuclei with DAPI and dead cell nuclei with propidium iodide.

2.12. mRNA extraction and quantitative real-time PCR

RNA was extracted in triplicates from iRECs embedded into four different microenvironments (Matrigel®, fibrin, collagen I and bioprinted) after 7 days of incubation, having 2D seeded iRECs as a control. In particular, each replicate corresponded to passages p35, p48 and p53, covering a time of six weeks in culture among biological replicates. For each condition, including the 2D control, 8 identical samples, produced at day 0 with 6000 cells each, were pooled for RNA extraction. For ADPKD experiments, *Pkd1* iREC lysates and whole kidney lysates of iPkd1 and control mice were used. Total RNA was extracted using the QIAzol Lysis Reagent (Qiagen, no. 79306), and isolated with the RNeasy Plus Universal Mini Kit (Qiagen, no. 73404), according to the manufacturer's instructions. For 3D hydrogels, initial steps suggested by Khetan and Burdick were applied [45]. To reversely transcribe 1 µg of total RNA to cDNA the QuantiTect ReverseTranscription Kit (Qiagen, no. 205311) was applied. Quantitative PCR was performed on a Roche LightCycler® 480 instrument using Takyon™SYBR®Master Mix (Eurogentec, Takyon™ No Rox SYBR®MasterMix dTTP Blue, UF-NSMT-B0701) or Light Cycler 480 SYBR Green I Master (Roche, no. 04707516001). Per reaction, 10 ng of cDNA template were applied. Primers used in this study are listed in Supplementary Table 1. Threshold cycle (CT) values were normalized to CT values of *Tbp* (TATA box binding protein) as housekeeping gene and analyzed applying the comparative CT method [46].

2.13. Transcriptomic analysis

For RNA sequencing, total RNA was extracted as described above. Library preparation and RNA sequencing were performed by Eurofinsgenomics (GATC Biotech AG, Konstanz) for *Pkd1* iREC samples and by Novogene (HK) for iREC samples. Respectively, single-end 50 bp mRNA reads and 150 bp paired-end reads were generated and sequenced on an Illumina HiSeq platform. Fastq files were uploaded to the Galaxy platform and further processed with the usegalaxy.eu server [47]. After quality check using FastQC (version 0.67 and 0.72) and read trimming with TrimGalore! (Version 0.4.3.0), reads were aligned to the genome build GRCm38.89 (mm10) with RNA STAR (version 2.5.2b-2 and 2.6.0b-1) [48]. For differential gene expression analysis, gene counts were computed with featureCounts (version 1.6.0.3 and 1.6.3) [49] and statistically evaluated with DESeq2 (version 1.22.1 and 2.11.40.1) [50]. The DESeq2 analysis for the 3D cultured iRECs was run considering each microenvironment and individual replicate as a factor. Further bioinformatic analysis and visualization were conducted with Rstudio (version March 1, 1093, R version 4.0.2). Kidney enrichment was determined for genes with an expression in the mouse kidney larger than the median of all other mouse tissues profiled in Shen Y. et al. [51]. The gene ontology (GO) enrichment analysis of *Pkd1* data was run with clusterProfiler (version 3.10.1) with a p-value cutoff of 0.01, corrected with the Benjamini–Hochberg method, and a q-value cutoff of 0.05 [52]. Further analyses were performed with the g:Profiler web version [53] (version: e101_eg48_p14_baf17f0, Benjamini-Hochberg FDR = 0.05) and the REVIGO platform [54]. Volcano plots and heatmaps were made with Bioconductor packages [55] and R packages ggplot2 (version 3.2.1), heatmap.plus (version 1.3), EnhancedVolcano (version 1.10.0), pheatmap (version 1.0.12) and scatterplot3d (version 0.3–41). Previously published RNA sequencing data were reanalyzed using the same processing algorithm on the usegalaxy.eu server as described above.

2.14. Statistical analysis

Data were statistically analyzed and visualized using GraphPad Prism8 (GraphPad, version 8.4.2) software. To test for normal distribution, Shapiro-Wilk and Kolmogorov-Smirnov tests were used. Biological and technical replicates were reported along with each experiment (N), together with the statistical test. When one-way or two-way Anova proved significant differences, relevant individual comparisons were tested (Sigma, GraphPad). Significance levels of statistical tests as indicated in the figures: n.s. - non-significant, *$p < 0.05$, ** <0.01, *** <0.001, **** <0.0001.

2.15. Western blotting

For Western blot analysis, protein lysates were extracted using lysis buffer (1% Triton-X 100, 20 mM Tris pH 7.5, 50 mM NaCl, 50 mM NaF, 15 mM Na$_4$P$_2$O$_7$, 0.1 mM EDTA pH 8.0, cOmplete™ Protease Inhibitor (Roche, REF 11697498001), 0.25 mM PMSF and 2 mM Na$_3$VO$_4$). Proteins were fractionated by SDS-PAGE. For immunoprecipitation, lysates were ultracentrifuged at 43000 rpm for 30 min at 4 °C and incubated with Anti-V5 beads at 4 °C overnight. After blotting, immunoprecipitates were stained with Anti-Flag antibody. Antibodies are listed in Supplementary Table 2.

3. Results

3.1. Selection of hydrogels and assessment of biocompatibility with iRECs

First, we assessed structural features of three biomaterials widely used for 3D cell culture and bioprinting, namely Matrigel, fibrin and collagen I [14,56]. Our selection was based on the approach to use tissue-like biopolymers, reflecting the physicochemical microenvironment in natural tissues [56]. Matrigel and fibrin matrices have excellent biocompatibility, and can be enzymatically degraded and modified by cells, providing a high degree of freedom for cellular self-assembly [57]. This also accounts for collagen I, which is the most abundant interstitial protein, with well-defined compositions and tunable properties by setting the protein concentration before crosslinking [58]. The stability of these hydrogels was assessed in the absence of cells over 10 days (Supplementary Figs. 1a, b, c). Matrigel showed initial swelling between day 1–4, while no weight loss was detected in comparison to its initial weight (Supplementary Fig. 1a). Weight loss and a subsequent degradation were more pronounced in fibrin, followed by collagen I, and ranged from 22.4 to 35.2% of initial weight at day 10. When hydrogels were incubated with iRECs (Fig. 1a and b), initial swelling was only observed in Matrigel, and weight loss of all hydrogels was accelerated (Supplementary Figs. 1a, b, c). The addition of cells led to the complete degradation of fibrin after 24–48 h. As previously shown [59], the serine protease inhibitor aprotinin was necessary to prevent premature hydrogel dissolution (Supplementary Fig. 1b).

We next evaluated the biocompatibility of Matrigel, fibrin and collagen I by measuring iREC viability with a live/dead assay (Supplementary Figs. 1d, e, f). In Matrigel and fibrin, a high iREC viability was maintained over 11 days, while it decreased significantly in collagen I (Supplementary Fig. 1f). Interestingly, cell survival also depended on the culture medium. On day 6, renal epithelial growth medium (REGM) showed a beneficial impact on cell survival compared to standard culture medium (MEFM) in Matrigel and collagen I. In fibrin, however, viability was significantly reduced when iRECs were incubated in REGM (Supplementary Fig. 1f).

3.2. iRECs self-assemble into complex structures depending on the embedding conditions

All hydrogel microenvironments promoted self-assembly of embedded cells into multicellular structures (Fig. 1c). However, each
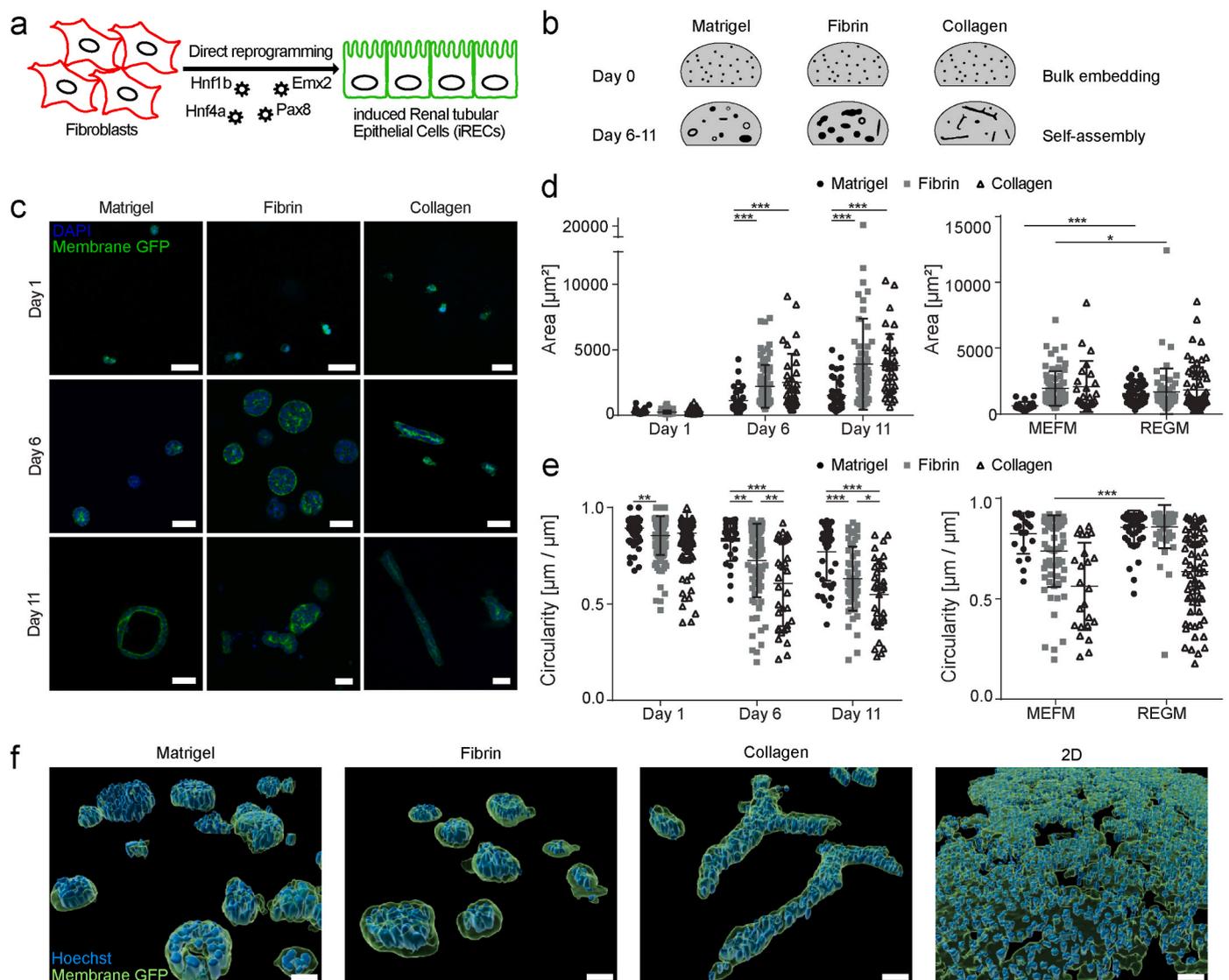
Fig. 1. iRECs show specific responses to embedding conditions and culture media. (a) Schematic of the direct reprogramming procedure to obtain murine iRECs. (b) Experimental layout of analyzed biomaterials (Matrigel, fibrin, collagen I). (c) Confocal images of embedded iRECs at indicated time points. Scale bars: 50 μm. (d,e) Geometrical quantification of iREC aggregates: area (d) and circularity (e) over time and in MEFM or REGM (*t*-test). (f) 3D reconstructions of deconvoluted z-stacks of embedded and 2D cultured iRECs at day 7. Scale bars: 50 μm.

hydrogel had a different impact on the number, size and morphology of iREC structures. Over 11 days, the number of self-assembled structures was highest in fibrin. In Matrigel and collagen I, the incubation of cells in REGM led to higher numbers of cell structures compared to MEFM (Supplementary Fig. 1g). In Matrigel, self-assembly of iRECs resulted in small aggregates with high sphericity. In fibrin, mostly spheroids and sporadic tubule-like aggregates were detected. Matrigel spheroids grew bigger in size in REGM (Fig. 1d, Supplementary Fig. 1h). In fibrin, the size of spheroids was only slightly decreased by REGM, and it led to a significant increase in circularity (Fig. 1e). Cell structures in collagen I were mainly characterized by elongated and branching tubular shapes when cultured in REGM for 7 days (Fig. 1e and f).

To further characterize the differential impact of hydrogels on embedded cells, we investigated the apico-basal polarization of iREC structures by ZO-1 staining. In Matrigel, it could be detected towards the apical side of spheroids that contained a lumen. In collagen I, the apico-basal polarization was only partially conserved, as ZO-1 accumulated in the core of tubular aggregates, which in most cases did not form lumen. In fibrin, however, ZO-1 staining was seen at the inner and outer boundaries of spheroids, hinting towards a disturbed apico-basal

polarization (Fig. 2a).

4. Transcriptional changes specific to matrigel, fibrin and collagen I

As iRECs are a directly reprogrammed kidney cell line originating from primary MEFs, we verified that cells maintained their differentiation status when incubated in 3D hydrogels. The expression levels of epithelial and kidney specific genes like *Cdh1* (adherens junctions), *Cdh16* (kidney specific protein), *Lrp2* (megalin, absorptive epithelial tissues) and *Slc17a1* (renal specific sodium-phosphate cotransporter) were measured in iRECs (Fig. 2b) at early (p24/p36) and late passages (p44/p53) separated by a culture period of 3 months. After 7 days in 2D or 3D culture, the gene expression of differentiation markers was maintained in both early and late passaged iRECs compared to primary MEFs. Thus, iRECs did not de-differentiate substantially over time or when cultured in 3D microenvironments. Comparing iRECs embedded in 3D microenvironments with 2D plated cells, we detected a significant upregulation of *Cdh1* in Matrigel and a downregulation of *Slc17a1* in fibrin (Fig. 2b). Therefore, the respective microenvironment had a small
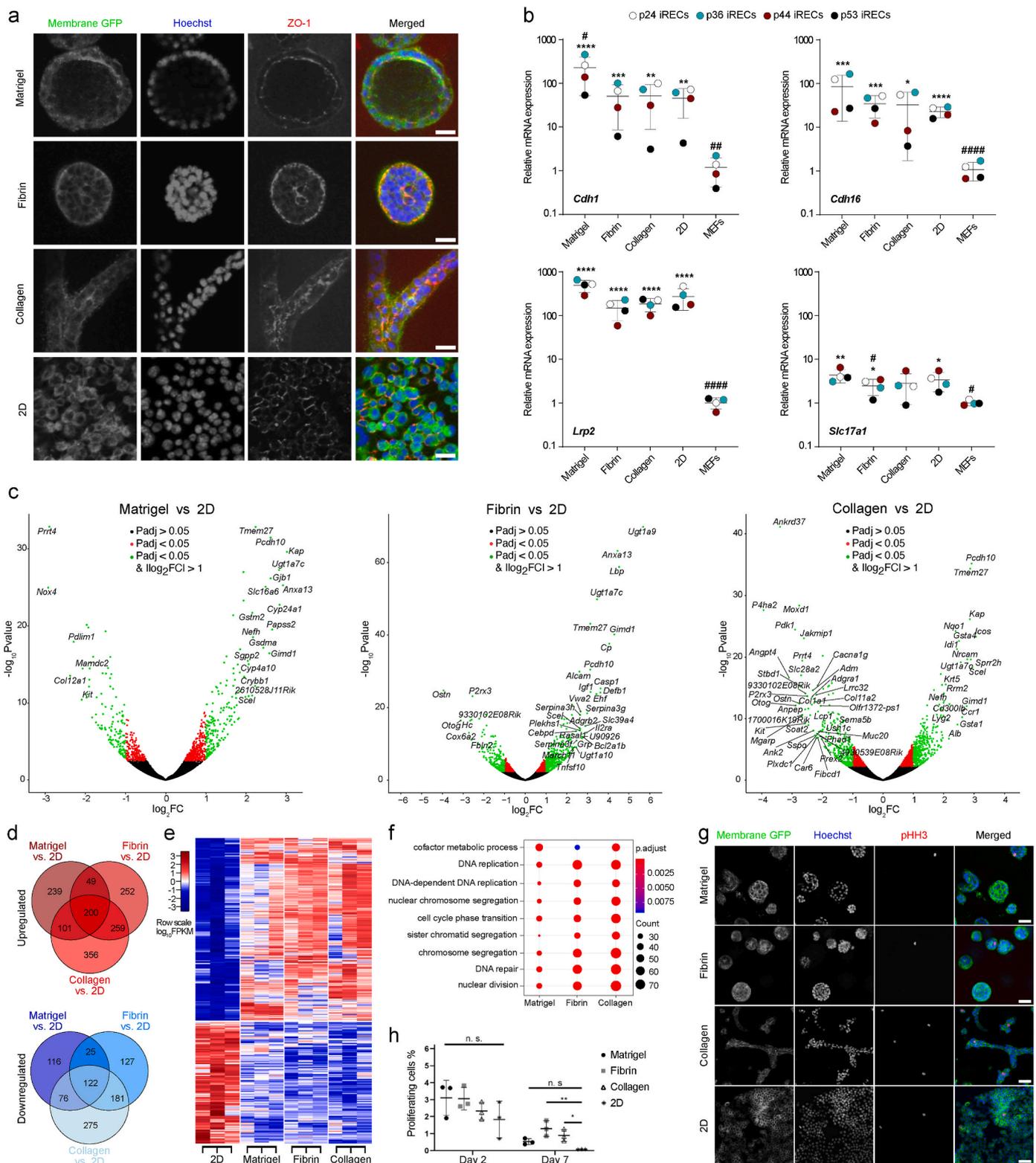
Fig. 2. Differentiation status and transcriptional response of iRECs in 3D culture. (a) Confocal images of iRECs immunostained on day 7. Scale bars: 20 μm. (b) RT-qPCR of tubule differentiation markers in iRECs embedded for 7 days in comparison to mouse embryonic fibroblasts (MEFs), significance reported by *, or in comparison to 2D iRECs (#), after 3 months in culture. N = 4 independent experiments (color-coded) with 3 technical replicates. Ratio paired *t*-test. (c) Volcano plots of iRECs in Matrigel, fibrin and collagen I versus 2D plated cells. (d) Venn diagrams of DEGs (up- and downregulated) in the 3 embedding conditions with respect to 2D plated cells. (e) Heatmap of commonly significantly (padj <0.05) upregulated (200) and downregulated (122) genes. (f) GO-analysis (biological processes) of commonly upregulated DEGs with respect to 2D iRECs. (g) Phospho histone H3 (pHH3) immunostaining of 3D embedded and 2D cultured iRECs at day 7 to assess proliferative behavior. Scale bars: 50 μm. (h) Quantification of proliferative cells among embedded and 2D cultured iRECs at day 2 and day 7 (N = 3 independent experiments, 10 technical replicates each, ANOVA, Sidak's correction for multiple comparisons). (For interpretation of the references to color in this figure legend, the reader is referred to the Web version of this article.)

but detectable influence on the expression of differentiation markers.

Next, we analyzed how the 3D microenvironment affected gene regulation and expression in iRECs across the transcriptome. We performed RNA sequencing of iRECs cultured in Matrigel, fibrin and collagen I for 7 days, and compared gene expression levels of 3D embedded cells to conventionally 2D plated iRECs (Fig. 2c). A total of 2356 genes were differentially regulated (DEGs) in all 3D versus 2D conditions (Matrigel/2D, fibrin/2D, collagen/2D). We identified 322 DEGs, which were concordantly up- or downregulated in all 3D microenvironments. Interestingly, 3D embedding mainly resulted in upregulation of genes, whereas the portion of downregulated genes was smaller in all three conditions (Fig. 2c, d, e).

A GO term analysis of the 200 commonly upregulated DEGs detected enrichment in terms like DNA replication, chromosome segregation, nuclear division and DNA repair, hinting towards enhanced proliferation rates of 3D embedded cells (Fig. 2f). Immunostaining against Phospho histone H3 Ser10 (pHH3) confirmed increased proliferation rates between 2D and 3D embedded cells at day 7 after hydrogel embedding in fibrin or collagen I (Fig. 2g and h, Supplementary Figs. 2a and b).

4.1. Bioprinting of alginate hydrogels

We evaluated how enhanced control of iREC dispensing in the bioprinting process could affect cell viability and characteristics. Because of its favorable biophysical characteristics, alginate was selected as a bio-ink to determine compatibility of iRECs to the printing process [60]. Alginate crosslinks in the presence of $CaCl_2$ ions and can be coupled to an RGD sequence, a tripeptide which enhances cell-matrix interaction and promotes cell proliferation and migration [61]. We took advantage of an established DoD bioprinting technique to generate microstructured alginate hydrogels [24].

First, we assessed the degradation rate of alginate hydrogels and their compatibility with the bioprinting process. Low alginate concentrations (1% w/v) maintained at least 50% of the initial hydrogel weight after 7 days in culture. As expected, higher concentrations (2% w/v) led to slower degradation (Δ weight = 50% at t = 7 days versus t = 14 days) (Supplementary Fig. 3a). Additionally, higher concentrations showed improved mechanical stability, exhibiting a significantly higher compression stress value at maximum deformation compared to 1% w/v samples (Supplementary Figs. 3b and c). As DoD bioprinting requires specific hydrogel viscosity (working range: 0.5–500 mPa*s), we measured the viscosity of 1% w/v alginate, 2% w/v alginate, and 2% w/v RGD-modified alginate. All three solutions met the bioprinter
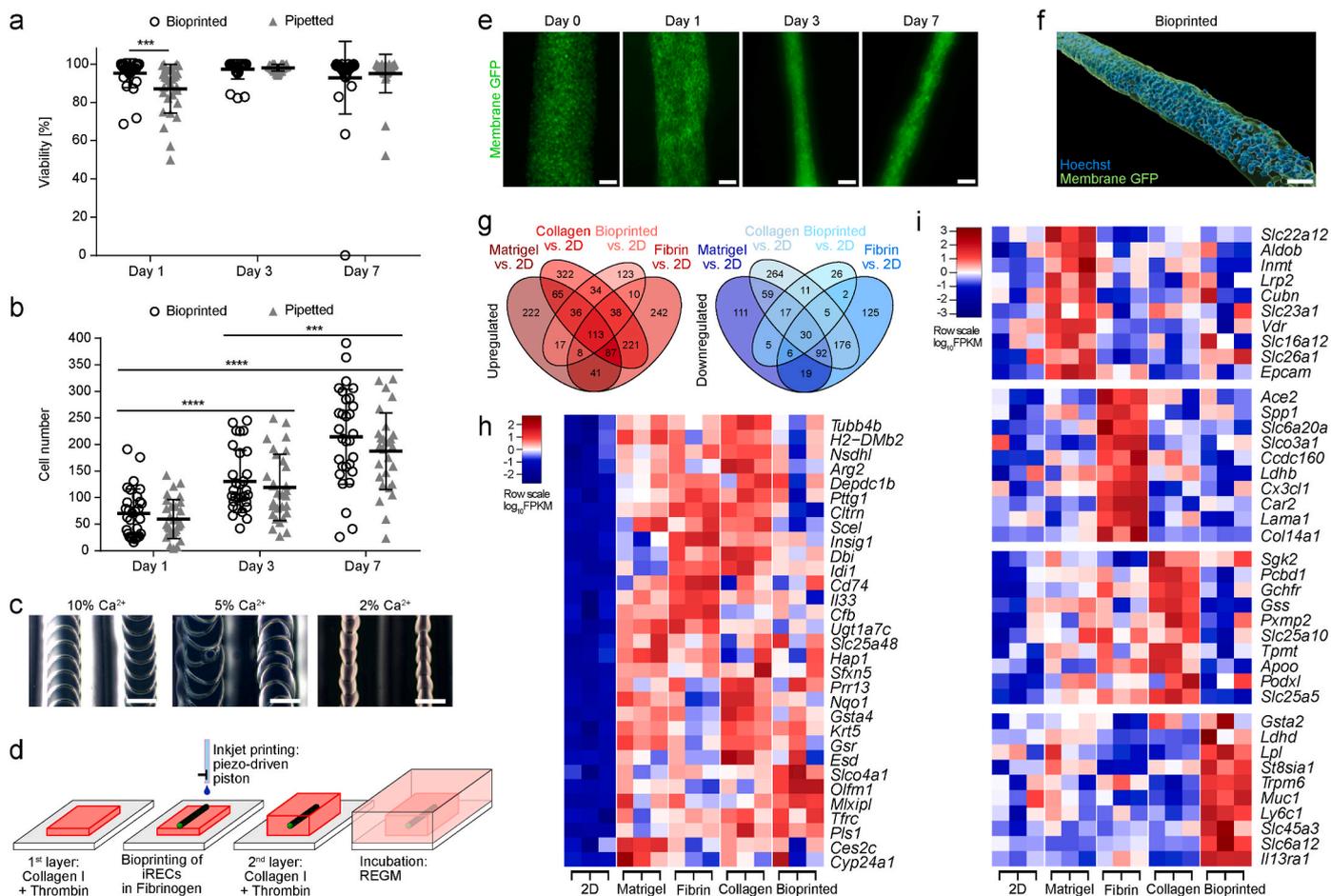

Fig. 3. iRECs can be biofabricated into a tubular pattern and activate a 3D microenvironment specific transcriptional program. (a) Quantification of viability and (b) proliferation of iRECs in alginate at indicated time points after bioprinting or manual pipetting (N = 30, 10 technical replicates from 3 independent experiments, Mann-Whitney *U* test). (c) Images of bioprinted alginate hydrogels cross-linked with increasing calcium ion concentrations, which formed a support matrix for embedded iRECs. Scale bars: 200 μm. (d) Schematic of the bioprinting procedure using fibrinogen-iREC deposition between two layers of collagen-thrombin. (e) Brightfield images of bioprinted GFP+ iREC samples over time showing self-assembly into narrower tubules. Scale bars: 100 μm. (f) 3D reconstruction of an iREC tubule 7 days after bioprinting. Scale bar: 50 μm. (g) Venn diagrams of up- and downregulated genes in 3D embedded or bioprinted microenvironments with respect to 2D iRECs. (h) Heatmap of commonly upregulated DEGs filtered for kidney enrichment. (i) Heatmap of the top ten DEGs uniquely upregulated in each microenvironment, filtered for kidney enrichment.

requirements (Supplementary Fig. 3d). Exhibiting sustained mechanical stability, we used 2% w/v alginate and RGD-alginate solutions for further experiments.

The biocompatibility of the DoD bioprinting technology with iRECs was analyzed by applying a live/dead assay. Interestingly, bioprinted cells displayed an increased viability (95.3 ± 7.4%) compared to manually dispensed cells (87.2 ± 12.6%) one day after bioprinting. Yet, both methods resulted in similar iREC viability after 3 and 7 days, respectively (Fig. 3a). Cell proliferation was detected at each timepoint, with no significant differences between bioprinted and manually pipetted conditions (Fig. 3b).

We compared the effect of three calcium chloride ($CaCl_2$) concentrations (2%, 5%, 10% w/v) on the printing process. When $CaCl_2$ was bioprinted on top of the alginate layer, the formation of a repetitive micropattern was observed, which could be modulated by altering the drop overlap distance (Supplementary Fig. 3e) and the crosslinker concentration (Fig. 3c). Multi-layered iRECs-containing alginate and RGD-alginate samples were generated, which showed a homogeneous distribution of cells (Supplementary Fig. 3f). Importantly, cells started to self-assemble and form 3D structures at day 7 in RGD-alginate samples, whereas they remained mostly singled in pristine alginate (Supplementary Figs. 3g and h). RGD-alginate improved the viability of cells after longer periods of incubation (day 21) (Supplementary Fig. 3i).

In conclusion, the automatic DoD dispensing process had no detrimental effect on printed iRECs. However, since iRECs remained mostly as single cells up to day 7 in both alginate and RGD-alginate, this biomaterial had to be excluded for further comparative analysis.

4.2. DoD bioprinting promotes formation of tubule-like iREC structures

Next, iRECs were bioprinted in a fibrin and collagen I matrix, arranged as a cell-containing layer of fibrin embedded between two layers of collagen I [24]. This enabled cells to self-assemble and to form tubule-like structures. As schematically shown in Fig. 3d, an iREC-fibrinogen suspension was bioprinted on top of a collagen I layer. The cell-containing bioink (fibrinogen) was dispensed as overlapping droplets by DoD based bioprinting with a droplet-to-droplet distance of 200 μm. As fibrinogen was enzymatically crosslinked to fibrin by thrombin, a serine protease contained in the first layer of collagen I, cells were positioned in a linear arrangement. Afterwards, a second layer of collagen I was printed on cell-laden fibrin, and the hydrogels were incubated in REGM for up to 10 days [24].

In contrast to alginate embedded cells, the bioprinted constructs in fibrin/collagen I formed a compact cell layer. This process of guided cellular self-assembly was already observed one day after printing (Fig. 3e). Subsequently, linear structures shrank in diameter and formed a three-dimensional tubule with a diameter of about 100 μm (Fig. 3e and f).

4.3. 3D microenvironments enhance nephron segment specificity

The transcriptome of bioprinted cells was analyzed after self-assembly to tubule-like structures at day 7 and compared to the profiles obtained from iRECs manually embedded in Matrigel, fibrin, and collagen I. 2483 genes were significantly differentially regulated with respect to 2D cultured iRECs (Supplementary Table 3). In the principal component analysis (PCA), bioprinted cells clustered separately from 2D cells. More importantly, they could be clearly distinguished from the other 3D microenvironments (Supplementary Fig. 4a). 113 DEGs were detected which were concordantly upregulated in all 4 conditions of 3D culture in comparison to 2D culture (Fig. 3g). Interestingly, 31 genes were kidney enriched, including *Tmem27* encoding collectrin, the amino acid transport regulator, or the sodium-independent organic anion transporter *Slco4a1* (Fig. 3h). Thus, this analysis identified a core set of genes that were differentially regulated in 3D cultured iRECs, independent of the embedding substrate.

We also detected substrate specific transcriptional changes that only occurred specifically in one of the embedding or printing conditions (Fig. 3i, Supplementary Fig. 4b). 60.5% of DEGs uniquely upregulated in Matrigel were kidney enriched, 30.2% in fibrin, 43.7% in collagen, and 45.3% in the bioprinted samples. Interestingly, the gene signature in Matrigel showed the strongest proximal tubular specificity with enhanced expression of *AldoB*, *Cubn*, or *Lrp2* and an accumulation of genes associated with the GO terms 'brush border' and 'apical membrane' (Supplementary Fig. 4c), also in comparison to the other microenvironments (Supplementary Fig. 4d). The urate transporter *Slc22a12* and the anion transporter *Slc26a1*, a nephrolithiasis risk locus, were significantly upregulated in Matrigel embedded samples.

Ace2 encoding for angiotensin converting enzyme 2, essential to the renal control of blood pressure and the functional receptor of SARS-CoV-2, was specifically upregulated in fibrin embedded iRECs. Among the transcripts with enhanced expression in collagen was *Pcbd1*, the Hnf1a co-factor, and the magnesium transporter *Trpm6* was found uniquely upregulated in the bioprinted sample. In conclusion, the different embedding conditions elicited specific transcriptomic responses with a surprisingly high number of kidney enriched genes in each of the differentially upregulated gene sets. The uniquely enhanced expression within each condition may allow tailoring the 3D culture conditions to specific experimental requirements and thereby even allow controlling certain tissue-specific functionalities.

4.4. Validation of differentially expressed genes

To correlate differential expression of transcripts with protein presence, a number of proteins encoded by genes commonly upregulated in 3D vs. 2D culture conditions was validated by immunofluorescence. Confirming the transcriptomic analysis, Nqo1, Arg2, and Olfm1 showed high and distinct protein expression in iRECs (Fig. 4a). In parallel, the renal tubule specific expression of respective genes was confirmed in adult mouse kidneys (Fig. 4b). Upregulation of *Slc25a48* and *Gsta4* was confirmed by RT-qPCR (Fig. 4c).

Similarly, we analyzed proteins encoded by genes with enhanced expression in only one condition. AldoB was upregulated in Matrigel and the expression unique to this condition was confirmed by immunofluorescence (Fig. 4d). The endogenous localization was restricted to proximal tubules, in line with a shift of iRECs towards a proximal transcriptomic profile in Matrigel (Fig. 4e). Spp1 was detected in fibrin embedded iRECs and nuclei of intermediate tubule segments. Podxl, which was upregulated in collagen, showed detectable immunostaining also in fibrin embedded samples and 2D cultured iRECs, thus partially confirming the RNA-Seq results. Immunostaining also confirmed the protein expression of Nqo1, Arg2 and Olfm1 in bioprinted samples. Trpm6, specifically enriched in the printed condition, was detectable at cell membranes (Fig. 4f).

4.5. Disease related genes are differentially regulated according to microenvironment

Among DEGs upregulated in at least one condition, genes were detected which are associated with or causative for renal diseases. These included tubulopathy related genes such as *Wnk4* (hyperkalemia) enhanced in Matrigel, *Car2* (pyelonephritis susceptibility) detected in fibrin, *Pcbd1* (hypomagnesemia and renal magnesium wasting) expressed in collagen or *Fxyd2* (Renal hypomagnesemia-2) found in collagen and the bioprinted samples (Fig. 4g). We conclude that *in vitro* models of renal diseases may be enhanced by employing culture conditions that favor the expression of respective genes.

4.6. Transcriptome analysis identifies a dysregulated gene signature in Pkd1 knockout iRECs

ADPKD is a highly prevalent genetic disease with a primary
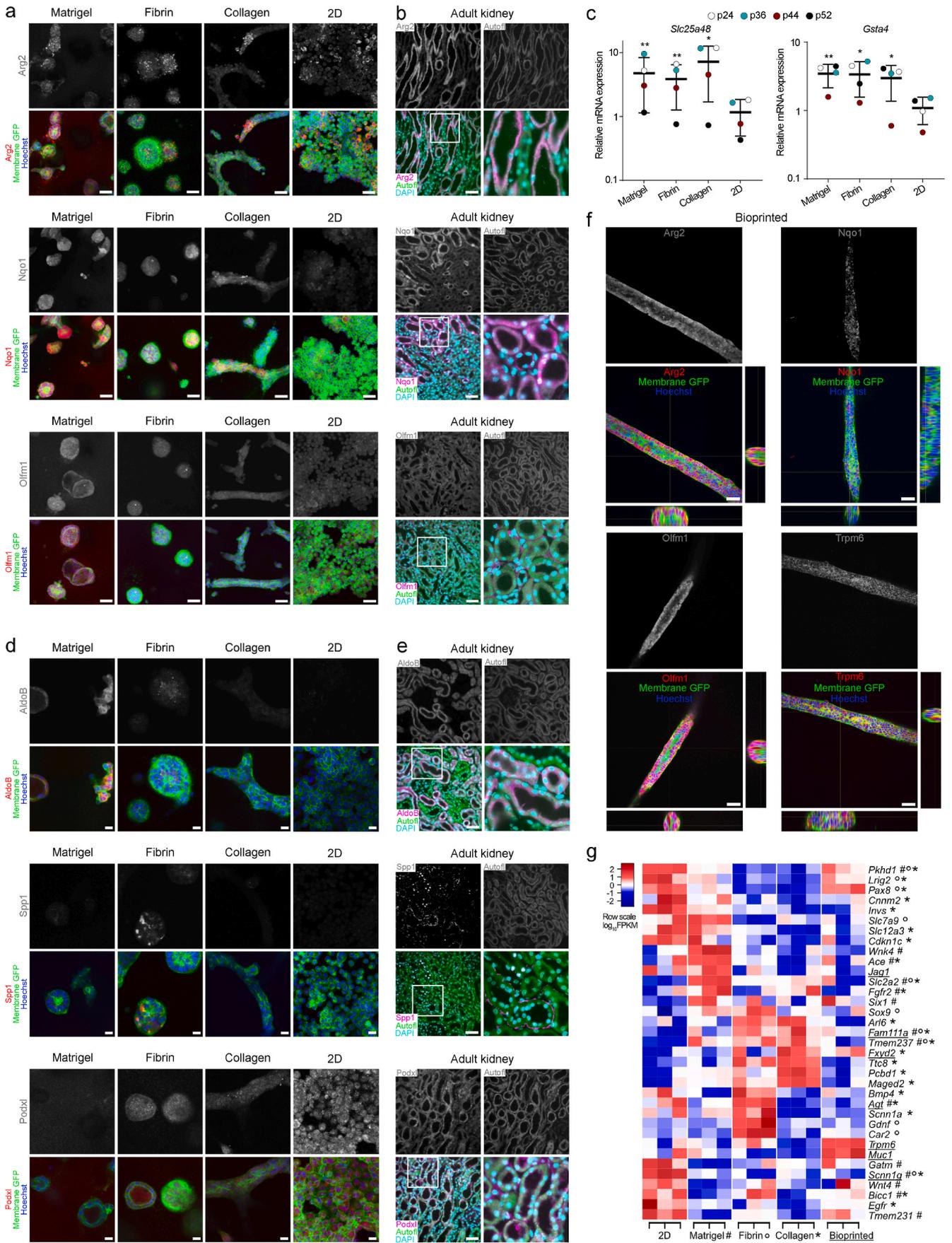
Fig. 4. Immunostaining confirms the presence of microenvironmental signature gene products. (a) Immunostaining of commonly upregulated proteins in hydrogel embedded iRECs vs. 2D. Maximum intensity projections of confocal z-stacks. Scale bars: 50 μm. (b) Immunohistochemistry of commonly upregulated proteins in WT mouse kidneys. Scale bars: 50 μm. (c) Relative mRNA quantification of commonly upregulated genes *Slc25a48* and *Gsta4* in 3D cultured iRECs vs. 2D control. N = 4 independent experiments (color-coded) with 3 technical replicates. Ratio paired *t*-test. (d) Immunostaining of proteins encoded by uniquely upregulated genes in 3D microenvironments with respect to 2D. Scale bars: 50 μm. (e) Localization of uniquely upregulated proteins in mouse kidney sections. Scale bars: 50 μm. (f) Immunostaining of commonly upregulated proteins (Arg2, Nqo1, Olfm1) and unique protein Trpm6 in the bioprinted sample. Maximum intensity projection of confocal z-stacks. Scale bars: 50 μm. (g) Heatmap of kidney disease related genes (padj <0.05 in at least one condition). # = significant in Matrigel vs. 2D, ° = significant in fibrin vs. 2D, * = significant in collagen vs. 2D, underlined = significant in bioprinted vs. 2D. (For interpretation of the references to color in this figure legend, the reader is referred to the Web version of this article.)

manifestation in renal tubular cells. We generated induced renal tubular epithelial cells with a loss-of-function allele for *Pkd1* and analyzed the cellular transcriptome and morphology in 3D culture (Fig. 5a). MEFs from mice homozygous for floxed *Pkd1* alleles were reprogrammed to *Pkd1*^fl/fl iRECs, clonally expanded, and their tubule-specific differentiation state was confirmed by RT-qPCR (Supplementary Fig. 5a). As each clone showed an individual composition of marker gene expression, we selected clones that maintained expression of a broad range of tubule specific markers. In total, 6 *Pkd1*^fl/fl clones were chosen. Each of these clones was transduced with Flippase (Flp) as control, and, in parallel, with Cre recombinase (Cre) to generate a *Pkd1* knockout, respectively. Hence, we could directly compare knockout cells to their corresponding wild-type clones. Cre recombination and knockout of *Pkd1* were confirmed by genotyping. The reduction of the *Pkd1* gene product PC1 was tested by Western blot analysis (Supplementary Figs. 5b and c).

Transcriptional changes were analyzed by RNA sequencing in 3 pairs of *Pkd1* clones. 303 DEGs were detected between control (Flp) and the Cre expressing cells. 121 genes were downregulated, and 182 genes were upregulated in *Pkd1* knockout clones. Overall, 21 DEGs had a fold change of >2 (Fig. 5b and c, Supplementary Table 4). As expected in the Cre condition, the expression level of *Pkd1* was reduced and no reads aligned to the genomic region of exons 2–4 of the *Pkd1* gene, confirming successful Cre recombination (Supplementary Fig. 5d). The functional enrichment analysis showed an accumulation of GO terms associated with epithelial development, e.g., cell-cell adhesion, transmembrane and ion transport, tube development, apoptotic signaling pathway, actin cytoskeleton organization, and urogenital system development (Supplementary Fig. 6a).

4.7. Comparison to other transcriptomes identifies a PC1 dependent induction of Aldh1a1

To further evaluate the findings made in reprogrammed renal tubular cells, the datasets were compared to publicly available RNA sequencing studies of two *Pkd1* knockout mouse models. We reanalyzed transcriptomic data of *Pkd1*^fl/fl;*HoxB7*-cre mice [62] and a tamoxifen inducible kidney-specific *Pkd1* deletion mouse model (iKsp-*Pkd1*^del) [63] by applying the same processing algorithms as used for iREC RNA sequencing (Fig. 5d and e, Supplementary Table 4). Interestingly, among 15 concordantly regulated genes found in all three datasets, the highest fold change could be found for *Aldh1a1* (*Pkd1* iRECs fold change (FC) = 2.07, *Pkd1*^fl/fl;*HoxB7* FC = 6.45, iKsp-*Pkd1*^del FC = 2.29, p_adj < 0.001).

We selected a list of overlapping genes found in the *Pkd1* knockout datasets and, for further validation, analyzed them by RT-qPCR. In parallel to *Pkd1* iRECs, we made use of RNA from an inducible *Pkd1* mouse model. Adult onset polycystic kidney disease was induced in *Pkd1*^fl/fl;*Pax8*^rtTA;*TetO*-cre mice (iPkd1 mice) by doxycycline treatment between P28 to P42 [39], and RNA was extracted at 12 weeks of age. The upregulation of *Aldh1a1* expression after *Pkd1* knockout could be confirmed in all iREC clones and the iPkd1 mouse model, where a significant upregulation of *Aldh1a1* was detected in comparison to wild-type littermates. Moreover, *Itga9*, *Slc16a10*, *Fbxo40*, *Heg1*, and *Pla1a* were also concordantly up- or downregulated in the iPkd1 model (Fig. 5f). For other genes, the *Pkd1* iREC RNA sequencing results could be confirmed by RT-qPCR, but results in iPkd1 mice were either non-significant or showed non-concordant regulation (Supplementary

Fig. 7a).

Next, we analyzed if differential regulation of selected genes found in the RNA sequencing datasets was directly dependent on *Pkd1* expression. Therefore, the *Pkd1* coding sequence was transduced retrovirally into *Pkd1* knockout iREC clones to rescue PC1 expression. Using an Anti-PC1 antibody, re-expression of PC1 could be confirmed in three *Pkd1* knockout clones (Supplementary Fig. 7b, upper line). As the *Pkd1* coding sequence in the retroviral vector was marked with an amino-terminal Flag tag and a carboxy-terminal V5 tag, immunoprecipitation was applied to check the expression of full-length PC1 protein (Supplementary Fig. 7b, lower line).

The expression level of several genes found in the *Pkd1* knockout datasets was determined after *Pkd1* rescue. Again, the higher mRNA level of *Aldh1a1* could be confirmed in three *Pkd1* knockout clones in relation to the corresponding wild-type clones, and *Aldh1a1* expression returned to wild-type levels in the rescue condition in each clone pair (Supplementary Fig. 7c). The reconstitution of the wild-type expression level was also observed for *Slc25a37*, *Serpine2*, *Heg1*, *Exoc5*, and *Itga9*. For other genes, the rescue yielded a non-significant result, or it showed an enhancement of deregulation (Fig. 5g, Supplementary Fig. 7d).

4.8. Bioprinting uncovers a tubular morphology defect not discernible in 2D culture

First, we checked the influence of *Pkd1* knockout on cell proliferation in 2D cell culture. All *Pkd1* iREC clones were grown in standard culture medium (DMEM) supplemented with 10% FBS. The knockout of *Pkd1* did not alter cell proliferation rates compared to corresponding wild-type clones during a one-week course (Supplementary Fig. 8a). Next, we focused on morphological features of *Pkd1* iRECs in 3D cell culture. 6 *Pkd1* iREC clone pairs were embedded in Matrigel and cultivated in Renal Epithelial Growth Medium (REGM) for up to 10 days. Cells were singled and seeded in low concentrations (100 cells μl^{-1}) to allow cell proliferation and formation of spheroids. Spheroid size and volume were determined, but no significant differences were detected between control (Flp) and *Pkd1* knockout (Cre) conditions (Fig. 6a and b and Supplementary Fig. 8b). *Pkd1* iREC clones were also seeded in hanging drop culture. Cells aggregated and evolved into spheroidal structures. Again, no significant differences were detected concerning area, perimeter, and circularity of hanging drop spheroids (Fig. 6c, Supplementary Fig. 8c).

To further explore the behavior of *Pkd1* knockout iRECs in a more tubule-like conformation, we employed the bioprinted tubule model depicted in Fig. 3d to obtain bioprinted samples of cell-containing fibrin matrix sandwiched between collagen I layers, analogously to the tubules analyzed earlier in this work [24]. Again, bioprinted cells started to form tubular aggregates after a few days in culture. In control (Flp) conditions, bioprinted cell aggregates developed into well-defined and sharply bounded tubule-like structures over time (Fig. 6d and e). Interestingly, two days after the printing process, *Pkd1* knockout (Cre) tubule-like structures started to develop lateral protrusions, which diverted from the main axis, mainly perpendicularly, and grew in length. This phenomenon was significantly more prominent in the Cre conditions. We performed bioprinting for all 6 *Pkd1* iREC clone pairs (Flp and Cre) and analyzed the number of side tubules per millimeter of main tubule, the cross-sectional dimension of the main tubule and the length of side tubules. In Cre conditions, the mean number of side
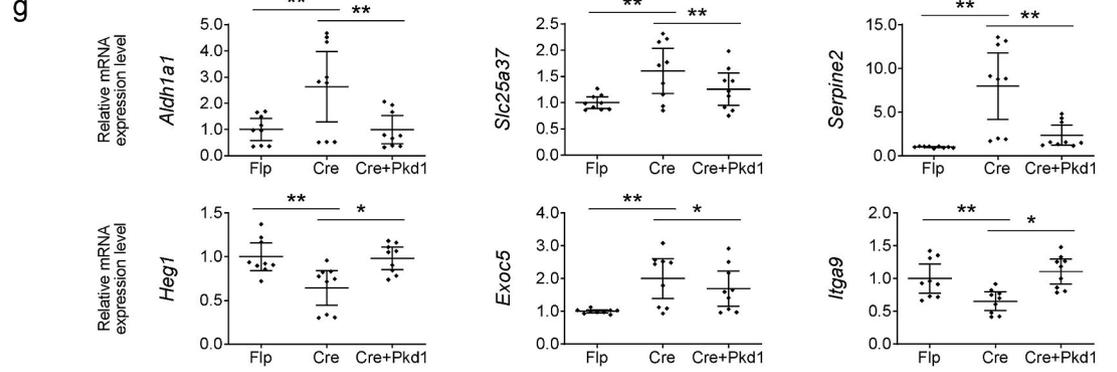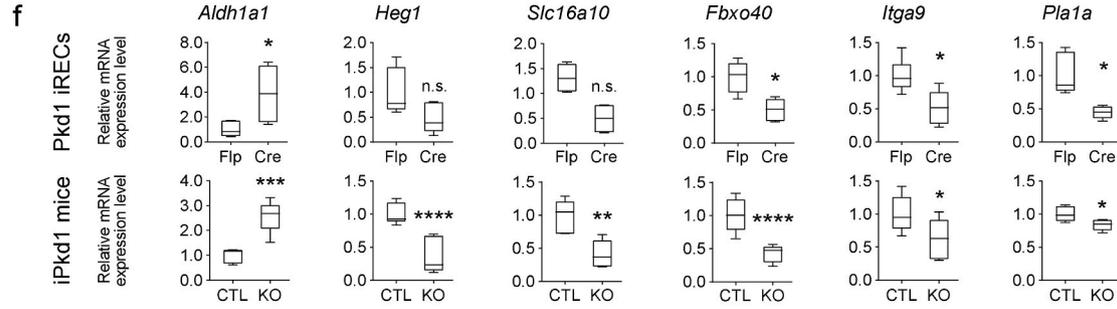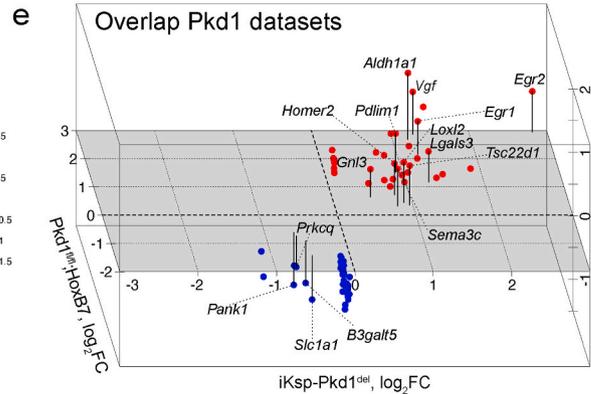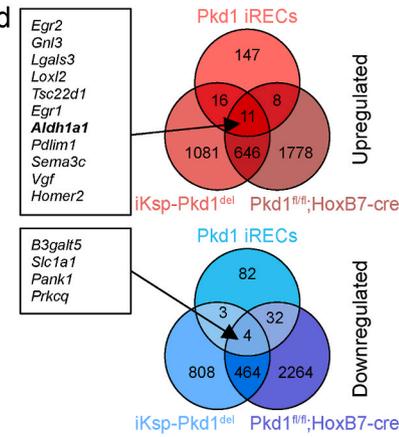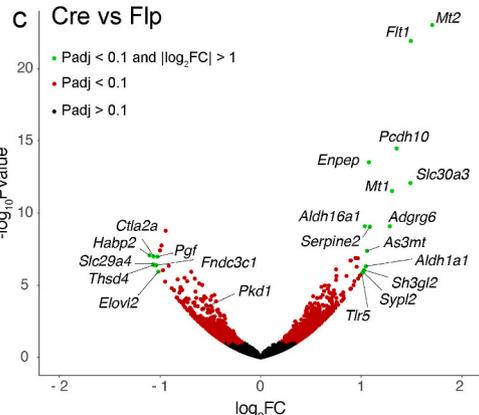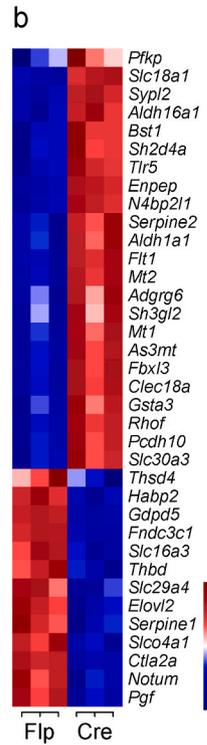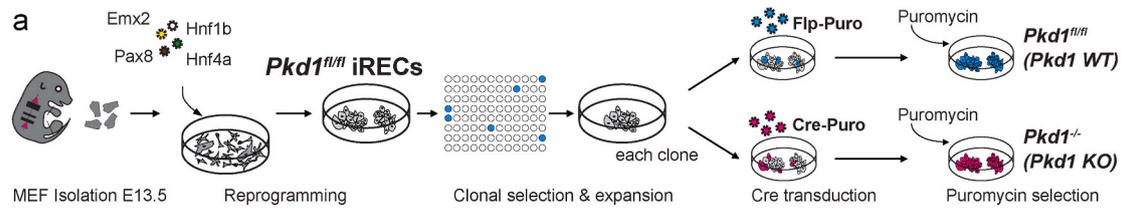
(caption on next page)

Fig. 5. *Pkd1* knockout iRECs differentially express genes that overlap with *in vivo* ADPKD models. (a) Schematic of the generation process of *Pkd1* knockout iRECs. (b) Heatmap of most prominent DEGs in *Pkd1* knockout iRECs detected by RNA sequencing ($p_{adj} < 0.001$) and volcano plot of the results (c). (d) Comparison of DEGs in $Pkd1^{-/-}$ iRECs with publicly available datasets. Venn diagrams: number of overlapping upregulated and downregulated genes. (e) 3D scatter plot, $\log_2$FC of overlapping genes in *Pkd1* datasets. (f) RT-qPCR analysis in iRECs and iPkd1 mice. Upper plots: relative mRNA expression levels of Flp and Cre conditions in *Pkd1* iRECs. Lower plots: corresponding mRNA expression levels in wild-type (CTL) and iPkd1 mice (KO). *Pkd1* iRECs: Wilcoxon matched pairs test, iPkd1 mice: Mann-Whitney *U* test. (g) RT-qPCR analysis of *Pkd1* iREC clones. *Pkd1* wild type: Flp; *Pkd1* knockout: Cre; *Pkd1* knockout with rescue: Cre + *Pkd1*. Wilcoxon matched pairs test.
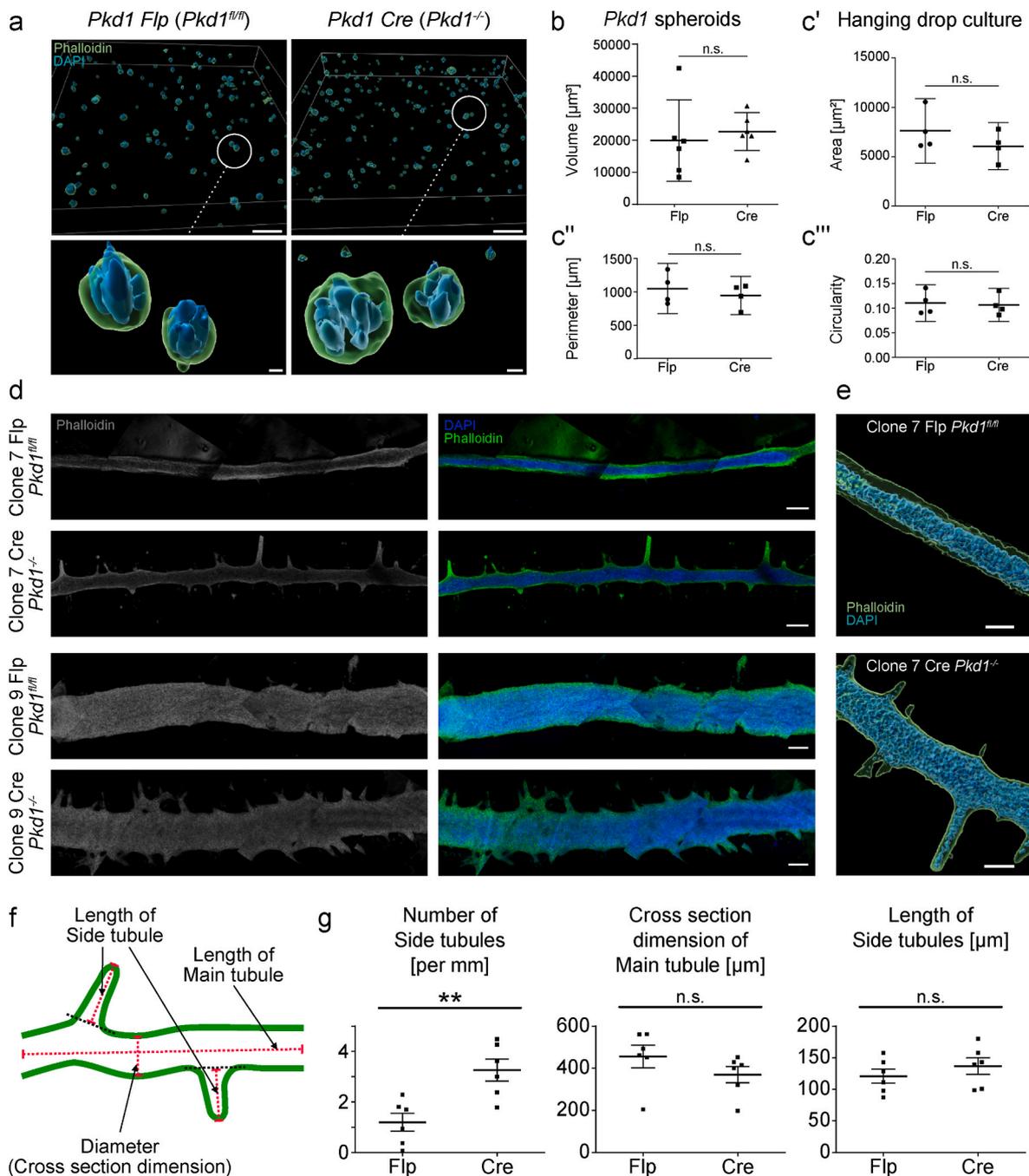

Fig. 6. Bioprinted tubules of $Pkd1^{-/-}$ iRECs reveal formation of radial extensions. (a) Confocal imaging of *Pkd1* clones embedded in Matrigel. Scale bars = 300 μm and 50 μm (zoomed spheroids). (b) Volume of *Pkd1* clones in [μm^3]. Flp (*Pkd1* WT), Cre (*Pkd1* KO). (c) (c') Area [μm^2], (c'') perimeter [μm], and (c''') circularity of hanging drop spheroids. (d) Representative images of tubule-like structures of *Pkd1* clones 7 and 9, Flp (*Pkd1* WT) and Cre (*Pkd1* KO) conditions. Scale bars = 200 μm. (e) 3D reconstruction of *Pkd1* tubules, clone 7 Flp and clone 7 Cre. Scale bars = 100 μm. (f) Schematic of tubule parameter measurements. (g) Quantification of tubule parameters: number of side tubules per mm of main tubule, diameter (cross section dimension) of main tubule [μm] and length of side tubules [μm]. N = 6 clone pairs, paired Student's t-test.

tubules per millimeter of main tubule exceeded the number of side tubules in Flp conditions significantly. No relevant differences could be detected concerning the mean diameter of the main tubule and the mean length of side tubules (Fig. 6f and g). In addition, we used second harmonic generation imaging to investigate the orientation of collagen I fibers in the microenvironment of side tubules. *Pkd1* wild-type clones showed an accumulation of collagen fibers in the vicinity of unbranched tubule boundaries, while in *Pkd1*$^{-/-}$ samples, fewer collagen I fibers were detected, and some fibers were aligned along the direction of tubular branching (Supplementary Fig. 9a).

We also detected alignment of the actin cytoskeleton following the direction of side tubule branching, as shown in a vector analysis of phalloidin staining (Supplementary Fig. 9b). Moreover, pHH3 staining indicated enhanced proliferative cell activity at the basis of and within side tubules (Supplementary Fig. 9c).

5. Discussion

Here, we investigated the influence of specific 3D microenvironments on the viability, gene expression profiles and morphological behavior of renal tubule-like cells (iRECs) generated by direct reprogramming embedded in fibrin, collagen I, and Matrigel. Considering that iRECs showed differential morphological and transcriptomic responses in the diverse microenvironments, we established a bioprinted tubular disease model using *Pkd1* knockout cells. This demonstrated a link to the retinoic acid synthetase *Aldh1a1* and uncovered disrupted tubular self-assembly mechanisms at the ECM-interface of PC1 depleted iRECs.

2D cell culture models cannot represent the complex architecture of renal tissues and thus fail to mimic disease states *in vitro*. Novel 3D models aim to replicate cell-matrix interactions and allow tissues to assume conformations that more closely resemble their *in vivo* state. In contrast to models based on iPSC derived renal organoids [64] or immortalized cell lines [21], we used directly reprogrammed cells. These combine two unique features that benefit the establishment of an *in vitro* tubule model: iRECs are proliferative and remain stably differentiated over many months in culture (up to 3 months) [5], even allowing for clonal expansion. Proliferation rates can be either inhibited or accelerated in a cell line and hydrogel dependent manner [65]. Remarkably, placing iRECs into 3D microenvironments further stimulated their growth into complex multicellular aggregates, independent of the specific embedding substrate.

Systematically comparing commonly used biomaterials as embedding substrates allowed us to identify specific cell responses. Both cellular morphology and transcriptional responses varied substantially depending on the different hydrogels. This suggests that iRECs display a considerable degree of plasticity influenced by their 3D microenvironment. Genes encoding for tubular transporters, such as *Slc22a12* (Oat4l), *Slc23a1* (Vitamin C transporter Svct1), or *Slc26a1* were strongly expressed in Matrigel embedded cells in comparison to 2D cultured iRECs, confirming high substrate specific responses. Matrigel enhanced a proximal tubular signature, and induced iREC aggregates to assume roundish spheroidal shapes, as did fibrin. In contrast, collagen led to a tubular morphology. Collagen cross-links into 10–200 nm thick fibrils [66], which might encourage iRECs to grow along the main direction of fibril organization and subsequently form an elongated shape. Among the uniquely differentially regulated genes in collagen embedded iRECs was Sgk2, a regulator of tubular transport activity [67,68]. We conclude that by choosing an appropriate microenvironment, cellular properties can be tuned to optimize experimental assays, such as enhanced expression of proteins of interest or regulatory components of cellular morphology. Our transcriptomic and morphological data across materials may provide a useful resource to identify and exploit such beneficial conditions.

Bioprinting approaches make it possible to position biomaterial ink or cell-laden bioinks and thus control the spatial organization of renal cells [21,64]. Here, we chose collagen as substrate because of its tubule

enhancing properties, and bioprinted a line of iRECs diluted in fibrin between two collagen layers. This proven bioprinting technique utilizes self-assembly mechanisms of iRECs and resulted in a defined geometrical structure with a sharp cell-matrix interface, likely achieved by the guidance cues of collagen fibrils [24]. Collagen fibrils are known to regulate vascular network formation when oriented in 3D endothelial cultures [69], and human bone marrow-derived mesenchymal stromal cells displayed enhanced chondrogenic differentiation potential when embedded in aligned collagen-tyramine bioinks [70]. Our transcriptomic analysis identified gene signatures uniquely enhanced in printed samples, such as the magnesium channel *Trpm6*. Thus, bioprinting offers a customizable tool for generating a defined tubular geometry. In contrast to casting a hollow tube or generating an artificial lumen using sacrificial ink that is later seeded with cells [21], harnessing the self-organizational capacities of iRECs resulted in tubular formations with dimensions much closer to the physiological values of renal tubules [24].

Here, we utilized this bioprinting approach as an appealing platform to phenotypically characterize *Pkd1*$^{-/-}$ iRECs. The tubular shape of bioprinted constructs allowed us to examine *Pkd1* knockout-induced deviations from this geometry, of which the formation of side branches was the most striking manifestation. The pathogenetic chain of events after second hit-induced PC1 loss can conceptually be broken down into loss of polarity, disruption of cell-matrix interactions and fluid accumulation [71,72]. The observed alterations in tubule geometry may thus reflect earliest disease manifestations and could be caused by disturbed cell-cell or cell-matrix interactions and a partially disorientated growth behavior. This hypothesis is supported by our findings of altered collagen I fiber reorientation in *Pkd1* knockout samples and thus represents an interesting entry point for further investigations. The microenvironment plays a crucial role at early stages of ADPKD cystogenesis, and kidney epithelia can remodel the microenvironment through migratory forces [35]. PC1 is proposed to act as a mechano-sensor and at cell-cell and cell-matrix contacts, where it modulates multiple signaling pathways, which may be cilia independent [73]. PC1 influences the interaction between the extracellular matrix and integrins [74] and modulates cell-cell adhesions [75]. Interestingly, PKD1$^{-/-}$ kidney organoids showed impaired contraction when embedded in collagen I droplets, but cystogenesis mainly occurs under conditions of low adhesion [35]. Partial orientation of Pkd1$^{-/-}$ cells along the axis of side tubules and enhanced proliferative activity could hint towards a microenvironment-driven adjustment of signaling pathways involved in processes like cell cycle or cell migration of PC1 deficient cells. Thus, our bioprinted tubular model may allow us to address if the underlying molecular alterations are due to disruption in signaling pathways such as planar cell polarity (PCP) and oriented cell division (OCD) [76,77], or Hippo signaling [78], which have been implicated in cyst formation. The lateral protrusions in our disease model are a consistent and striking phenotype, which can be used as an experimental read-out for other ADPKD specific questions. Due to the scalability of bioprinting, pharmacological screening could be envisioned.

An additional finding was the upregulation of the retinoic acid synthesizing enzyme *Aldh1a1* in Pkd1$^{-/-}$ iRECs, consistent with published transcriptomes of multiple *in vivo* samples [62,63,79], which we independently confirmed. Aldh1a1 and RA signaling seem to enhance repair mechanisms after acute kidney injury [80]. The expression of Aldh1a isoenzymes switches from Aldh1a2, which is dominant in the fetal period, to Aldh1a1 postnatally [81]. *Aldh1a1*$^{-/-}$ mutant mice do not display defects in nephrogenesis [82], but are more susceptible to oxidative damage [83] and show metabolic alterations of adipogenesis, lipid metabolism and gluconeogenesis [84,85]. The *PKD1* promoter, located 200 bp upstream of the transcription start site, can be activated by retinoic acid via the Sp1 transcription factor [86], suggesting a potential regulatory control of RA. Representing a key enzyme in RA production, Aldh1a1 could be a potential disease modifier of ADPKD. Further studies are required to characterize the role of Aldh1a1 in

healthy and ADPKD kidneys, and to determine if the knockout of *Aldh1a1* mitigates the course of cystic kidney disease.

As animal models or renal organoids can make it difficult to differentiate confounding effects from inflammation, fibrosis or secondary tubular damage, our model allows a more focused analysis of tubule specific alterations. Our findings may thus be more relevant to the initial cystogenesis triggered by a loss of PC1 and warrant further investigation.

Credit author statement

Roman Pichler: Methodology, Visualization, Investigation, Validation, Data Curation, Formal Analysis, Writing- Original draft preparation, Writing- Reviewing and Editing, Ludovica Rizzo: Methodology, Visualization, Investigation, Validation, Data Curation, Formal Analysis, Writing- Original draft preparation, Writing- Reviewing and Editing, Kevin Tröndle: Methodology, Visualization, Investigation, Validation, Writing- Reviewing and Editing, Michaela Bühler: Investigation, Hanna Brucker: Investigation, Anna-Lena Müller: Investigation, Kelli Grand: Investigation, Data Curation, Silvia Farè: Investigation, Amandine Viau: Resources, Michael M. Kaminski: Investigation, E. Wolfgang Kuehn: Supervision, Funding acquisition, Fritz Koch: Investigation, Stefan Zimmermann: Supervision, Funding acquisition, Peter Koltay: Supervision, Funding acquisition, Soeren S. Lienkamp: Conceptualization, Supervision, Funding acquisition, Writing- Original draft preparation, Writing- Reviewing and Editing.

Declaration of competing interest

The authors declare that they have no known competing financial interests or personal relationships that could have appeared to influence the work reported in this paper.

Data availability

Data will be made available on request.

Acknowledgments

Appendix A. Supplementary data

Supplementary data to this article can be found online at https://doi. org/10.1016/j.biomaterials.2022.121910.

References

[1] S. Zhuang, M. Duan, Y. Yan, Src family kinases regulate renal epithelial dedifferentiation through activation of EGFR/PI3K signaling, J. Cell. Physiol. 227 (2012) 2138–2144.

[2] B.S. Cummings, J.M. Lasker, L.H. Lash, Expression of glutathione-dependent enzymes and cytochrome P450s in freshly isolated and primary cultures of proximal tubular cells from human kidney, J. Pharmacol. Exp. Therapeut. 293 (2000) 677–685.

[3] S.E. Jenkinson, et al., The limitations of renal epithelial cell line HK-2 as a model of drug transporter expression and function in the proximal tubule, Pflueg. Arch. Eur. J. Physiol. 464 (2012) 601–611.

[4] C. Lipps, T. May, H. Hauser, D. Wirth, Eternity and functionality – rational access to physiologically relevant cell lines, Biol. Chem. 394 (2013) 1637–1648.

[5] M.M. Kaminski, et al., Direct reprogramming of fibroblasts into renal tubular epithelial cells by defined transcription factors, Nat. Cell Biol. 18 (2016) 1269–1280.

[6] M.M. Kaminski, J. Tosic, R. Pichler, S.J. Arnold, S.S. Lienkamp, Engineering kidney cells: reprogramming and directed differentiation to renal tissues, Cell Tissue Res. 369 (2017) 185–197.

[7] J. Nicolas, et al., 3D extracellular matrix mimics: fundamental concepts and role of materials chemistry to influence stem cell fate, Biomacromolecules 21 (2020) 1968–1994.

[8] S. Kishi, T. Matsumoto, T. Ichimura, C.R. Brooks, Human reconstructed kidney models, In Vitro Cell. Dev. Biol. Anim. 57 (2021) 133–147.

[9] B.M. Baker, C.S. Chen, Deconstructing the third dimension – how 3D culture microenvironments alter cellular cues, J. Cell Sci. 125 (2012) 3015–3024.

[10] S.C. Ramaiahgari, et al., A 3D in vitro model of differentiated HepG2 cell spheroids with improved liver-like properties for repeated dose high-throughput toxicity studies, Arch. Toxicol. 88 (2014) 1083–1095.

[11] H. Tekin, et al., Effects of 3D culturing conditions on the transcriptomic profile of stem-cell-derived neurons, Nat. Biomed. Eng. 2 (2018) 540–554.

[12] X. Wang, Advanced polymers for three-dimensional (3D) organ bioprinting, Micromachines 10 (2019) 814.

[13] U. Jammalamadaka, K. Tappa, Recent advances in biomaterials for 3D printing and tissue engineering, J. Funct. Biomater. 9 (2018) 22.

[14] M.F.J. Fransen, et al., Bioprinting of kidney in vitro models: cells, biomaterials, and manufacturing techniques, Essays Biochem. 65 (2021) 587–602.

[15] S.F. Bensamoun, L. Robert, G.E. Leclerc, L. Debernard, F. Charleux, Stiffness imaging of the kidney and adjacent abdominal tissues measured simultaneously using magnetic resonance elastography, Clin. Imag. 35 (2011) 284–287.

[16] K. Jansen, C.C.L. Schuurmans, J. Jansen, R. Masereeuw, T. Vermonden, Hydrogel-based cell therapies for kidney regeneration: current trends in biofabrication and in vivo repair, Curr. Pharmaceut. Des. 23 (2017) 3845–3857.

[17] J.M. Unagolla, A.C. Jayasuriya, Hydrogel-based 3D bioprinting: a comprehensive review on cell-laden hydrogels, bioink formulations, and future perspectives, Appl. Mater. Today 18 (2020), 100479.

[18] J. Su, S.C. Satchell, R.N. Shah, J.A. Wertheim, Kidney decellularized extracellular matrix hydrogels: rheological characterization and human glomerular endothelial cell response to encapsulation, J. Biomed. Mater. Res. 106 (2018) 2448–2462.

[19] M. Adelfio, S. Szymkowiak, D.L. Kaplan, Matrigel-free laminin–entactin matrix to induce human renal proximal tubule structure formation in vitro, ACS Biomater. Sci. Eng. 6 (2020) 6618–6625.

[20] E. Axpe, M.L. Oyen, Applications of alginate-based bioinks in 3D bioprinting, Int. J. Mol. Sci. 17 (2016) 1976.

[21] N.Y.C. Lin, et al., Renal reabsorption in 3D vascularized proximal tubule models, Proc. Natl. Acad. Sci. U.S.A. 116 (2019) 5399–5404.

[22] H. Gudapati, M. Dey, I. Ozbolat, A comprehensive review on droplet-based bioprinting: past, present and future, Biomaterials 102 (2016) 20–42.

[23] N.K. Singh, et al., Three-dimensional cell-printing of advanced renal tubular tissue analogue, Biomaterials 232 (2020), 119734.

[24] K. Tröndle, et al., Scalable fabrication of renal spheroids and nephron-like tubules by bioprinting and controlled self-assembly of epithelial cells, Biofabrication 13 (2021), 035019.

[25] A.B. Chapman, et al., Autosomal-dominant polycystic kidney disease (ADPKD): executive summary from a kidney disease: improving global outcomes (KDIGO) controversies conference, Kidney Int. 88 (2015) 17–27.

[26] V.E. Torres, P.C. Harris, Y. Pirson, Autosomal dominant polycystic kidney disease, Lancet 369 (2007) 1287–1301.

[27] V.H. Gattone, X. Wang, P.C. Harris, V.E. Torres, Inhibition of renal cystic disease development and progression by a vasopressin V2 receptor antagonist, Nat. Med. 9 (2003) 1323–1326.

[28] G. Wu, et al., Somatic inactivation of Pkd2 results in polycystic kidney disease, Cell 93 (1998) 177–188.

[29] A.B. Chapman, Approaches to testing new treatments in autosomal dominant polycystic kidney disease: insights from the CRISP and HALT-PKD studies, Clin. J. Am. Soc. Nephrol. 3 (2008) 1197–1204.

[30] I.S.L. Leeuwen, et al., Lowering of Pkd1 expression is sufficient to cause polycystic kidney disease, Hum. Mol. Genet. 13 (2004) 3069–3077.

[31] S. Koslowski, C. Latapy, P. Auvray, M. Blondel, L. Meijer, An overview of in vivo and in vitro models for autosomal dominant polycystic kidney disease: a journey from 3D-cysts to mini-pigs, Int. J. Mol. Sci. 21 (2020) 4537.

[32] M. Sharma, G.A. Reif, D.P. Wallace, Chapter 5 - in vitro cyst formation of ADPKD cells, in: T. Weimbs (Ed.), Methods in Cell Biology, Academic Press, 2019, pp. 153 93–153111.

[33] E.E. Dixon, et al., GDNF drives rapid tubule morphogenesis in a novel 3D in vitro model for ADPKD, J. Cell Sci. 133 (2020).

[34] B.S. Freedman, et al., Modelling kidney disease with CRISPR-mutant kidney organoids derived from human pluripotent epiblast spheroids, Nat. Commun. 6 (2015) 8715.

[35] N.M. Cruz, et al., Organoid cystogenesis reveals a critical role of microenvironment in human polycystic kidney disease, Nat. Mater. 16 (2017) 1112–1119.

[36] Y. Shamshirgaran, et al., Rapid target validation in a Cas9-inducible hiPSC derived kidney model, Sci. Rep. 11 (2021), 16532.

[37] T. Shimizu, et al., A novel ADPKD model using kidney organoids derived from disease-specific human iPSCs, Biochem. Biophys. Res. Commun. 529 (2020) 1186–1194.

[38] K.B. Piontek, et al., A functional floxed allele of Pkd1 that can be conditionally inactivated in vivo, J. Am. Soc. Nephrol. 15 (2004) 3035–3043.

[39] M. Ma, X. Tian, P. Igarashi, G.J. Pazour, S. Somlo, Loss of cilia suppresses cyst growth in genetic models of autosomal dominant polycystic kidney disease, Nat. Genet. 45 (2013) 1004–1012.

[40] R.H. Kutner, X.Y. Zhang, J. Reiser, Production, concentration and titration of pseudotyped HIV-1-based lentiviral vectors, Nat. Protoc. 4 (2009) 495–505.

[41] B. Bioprinting Derby, Inkjet printing proteins and hybrid cell-containing materials and structures, J. Mater. Chem. 18 (2008) 5717–5721.

[42] X. Chen, O. Nadiarynkh, S. Plotnikov, P.J. Campagnola, Second harmonic generation microscopy for quantitative analysis of collagen fibrillar structure, Nat. Protoc. 7 (2012) 654–669.

[43] Z. Püspöki, M. Storath, D. Sage, M. Unser, Transforms and operators for directional bioimage analysis: a survey, in: W.H. De Vos, S. Munck, J.-P. Timmermans (Eds.), Focus on Bio-Image Informatics, vols. 69–93, Springer International Publishing, 2016, https://doi.org/10.1007/978-3-319-28549-8_3.

[44] K. Troendle, et al., Bioprinting of high cell-density constructs leads to controlled lumen formation with self-assembly of endothelial cells, J. Tissue Eng. Regen. Med. 13 (2019) 1883–1895.

[45] S. Khetan, J. Burdick, Cellular encapsulation in 3D hydrogels for tissue engineering, JoVE J. Vis. Exp. e1590 (2009).

[46] T.D. Schmittgen, K.J. Livak, Analyzing real-time PCR data by the comparative C(T) method, Nat. Protoc. 3 (2008) 1101–1108.

[47] E. Afgan, et al., The Galaxy platform for accessible, reproducible and collaborative biomedical analyses: 2018 update, Nucleic Acids Res. 46 (2018) W537–W544.

[48] A. Dobin, et al., STAR: ultrafast universal RNA-seq aligner, Bioinformatics 29 (2013) 15–21.

[49] Y. Liao, G.K. Smyth, W. Shi, featureCounts: an efficient general purpose program for assigning sequence reads to genomic features, Bioinformatics 30 (2014) 923–930.

[50] M.I. Love, W. Huber, S. Anders, Moderated estimation of fold change and dispersion for RNA-seq data with DESeq2, Genome Biol. 15 (2014) 550.

[51] Y. Shen, et al., A map of the cis-regulatory sequences in the mouse genome, Nature 488 (2012) 116–120.

[52] G. Yu, L.-G. Wang, Y. Han, Q.-Y. He, clusterProfiler: an R Package for comparing biological themes among gene clusters, OMICS A J. Integr. Biol. 16 (2012) 284–287.

[53] U. Raudvere, et al., Profiler: a web server for functional enrichment analysis and conversions of gene lists (2019 update), Nucleic Acids Res. 47 (2019) W191–W198.

[54] F. Supek, M. Bosnjak, N. Skunca, T. Smuc, REVIGO summarizes and visualizes long lists of gene ontology terms, PLoS One 6 (2011), e21800.

[55] W. Huber, et al., Orchestrating high-throughput genomic analysis with Bioconductor, Nat. Methods 12 (2015) 115–121.

[56] L. Benning, et al., Assessment of hydrogels for bioprinting of endothelial cells, J. Biomed. Mater. Res. 106 (2018) 935–947.

[57] C.H. Park, K.M. Woo, Fibrin-based biomaterial applications in tissue engineering and regenerative medicine, Adv. Exp. Med. Biol. 1064 (2018) 253–261.

[58] R. Parenteau-Bareil, R. Gauvin, F. Berthod, Collagen-based biomaterials for tissue engineering applications, Materials 3 (2010) 1863–1887.

[59] S.M. Willerth, K.J. Arendas, D.I. Gottlieb, S.E. Sakiyama-Elbert, Optimization of fibrin scaffolds for differentiation of murine embryonic stem cells into neural lineage cells, Biomaterials 27 (2006) 5990–6003.

[60] M.I. Neves, L. Moroni, C.C. Barrias, Modulating alginate hydrogels for improved biological performance as cellular 3D microenvironments, Front. Bioeng. Biotechnol. 8 (2020).

[61] J.A. Rowley, G. Madlambayan, D.J. Mooney, Alginate hydrogels as synthetic extracellular matrix materials, Biomaterials 20 (1999) 45–53.

[62] Y.M. Woo, et al., Profiling of miRNAs and target genes related to cystogenesis in ADPKD mouse models, Sci. Rep. 7 (2017), 14151.

[63] T.B. Malas, et al., Meta-analysis of polycystic kidney disease expression profiles defines strong involvement of injury repair processes, Am. J. Physiol. Ren. Physiol. 312 (2017) F806–F817.

[64] K.T. Lawlor, et al., Cellular extrusion bioprinting improves kidney organoid reproducibility and conformation, Nat. Mater. 20 (2021) 260–271.

[65] R. Edmondson, J.J. Broglie, A.F. Adcock, L. Yang, Three-dimensional cell culture systems and their applications in drug discovery and cell-based biosensors, Assay Drug Dev. Technol. 12 (2014) 207–218.

[66] P. Fratzl, Collagen: structure and mechanics, an introduction, in: P. Fratzl (Ed.), Collagen: Structure and Mechanics, 1–13, Springer US, 2008.

[67] N. Gamper, et al., K+ channel activation by all three isoforms of serum- and glucocorticoid-dependent protein kinase SGK, Pflügers Archiv 445 (2002) 60–66.

[68] H. Wang, D. Xu, M.F. Toh, A.C. Pao, G. You, Serum- and glucocorticoid-inducible kinase SGK2 regulates human organic anion transporters 4 via ubiquitin ligase Nedd4-2, Biochem. Pharmacol. 102 (2016) 120–129.

[69] M.G. McCoy, et al., Collagen fiber orientation regulates 3D vascular network formation and alignment, ACS Biomater. Sci. Eng. 4 (2018) 2967–2976.

[70] A. Schwab, et al., Tissue mimetic hyaluronan bioink containing collagen fibers with controlled orientation modulating cell migration and alignment, Mater. Today Bio 7 (2020), 100058.

[71] E.E. Dixon, O.M. Woodward, Three-dimensional in vitro models answer the right questions in ADPKD cystogenesis, Am. J. Physiol. Ren. Physiol. 315 (2018) F332–F335.

[72] I.A. Drummond, Polycystins, focal adhesions and extracellular matrix interactions, Biochim. Biophys. Acta BBA - Mol. Basis Dis. 1812 (2011) 1322–1326.

[73] M.C. Hogan, et al., Characterization of PKD protein-positive exosome-like vesicles, J. Am. Soc. Nephrol. 20 (2009) 278–288.

[74] K. Lee, S. Boctor, L.M.C. Barisoni, G.L. Gusella, Inactivation of integrin-β 1 prevents the development of polycystic kidney disease after the loss of polycystin-1, J. Am. Soc. Nephrol. 26 (2015) 888–895.

[75] M. Silberberg, A.J. Charron, R. Bacallao, A. Wandinger-Ness, Mispolarization of desmosomal proteins and altered intercellular adhesion in autosomal dominant polycystic kidney disease, Am. J. Physiol. Ren. Physiol. 288 (2005) F1153–F1163.

[76] A. Luyten, et al., Aberrant regulation of planar cell polarity in polycystic kidney disease, J. Am. Soc. Nephrol. 21 (2010) 1521–1532.

[77] K. Kunimoto, et al., Disruption of core planar cell polarity signaling regulates renal tubule morphogenesis but is not cystogenic, Curr. Biol. 27 (2017) 3120–3131.

[78] H. Happe, et al., Altered Hippo signalling in polycystic kidney disease, J. Pathol. 224 (2011) 133–142.

[79] W.C. Chen, Y.S. Tzeng, H. Li, Gene expression in early and progression phases of autosomal dominant polycystic kidney disease, BMC Res. Notes 1 (2008) 131.

[80] T.A. Yakulov, et al., CXCL12 and MYC control energy metabolism to support adaptive responses after kidney injury, Nat. Commun. 9 (2018) 3660.

[81] K. Niederreither, V. Fraulob, J.M. Garnier, P. Chambon, P. Dolle, Differential expression of retinoic acid-synthesizing (RALDH) enzymes during fetal development and organ differentiation in the mouse, Mech. Dev. 110 (2002) 165–171.

[82] X. Fan, et al., Targeted disruption of *Aldh1a1* (*Raldh1*) provides evidence for a complex mechanism of retinoic acid synthesis in the developing retina, Mol. Cell Biol. 23 (2003) 4637–4648.

[83] N. Lassen, et al., Multiple and additive functions of ALDH3A1 and ALDH1A1, J. Biol. Chem. 282 (2007) 25668–25676.

[84] O. Ziouzenkova, et al., Retinaldehyde represses adipogenesis and diet-induced obesity, Nat. Med. 13 (2007) 695–702.

[85] F.W. Kiefer, et al., Retinaldehyde dehydrogenase 1 coordinates hepatic gluconeogenesis and lipid metabolism, Endocrinology 153 (2012) 3089–3099.

[86] M.R. Islam, et al., Retinoic acid-dependent activation of the polycystic kidney disease-1 (PKD1) promoter, Am. J. Physiol. Ren. Physiol. 295 (2008) F1845–F1854.